Multiscale Hazard Scenarios

Regional seismic hazard scenarios (ground motion at bedrock)

Regional Scale - NDSHA

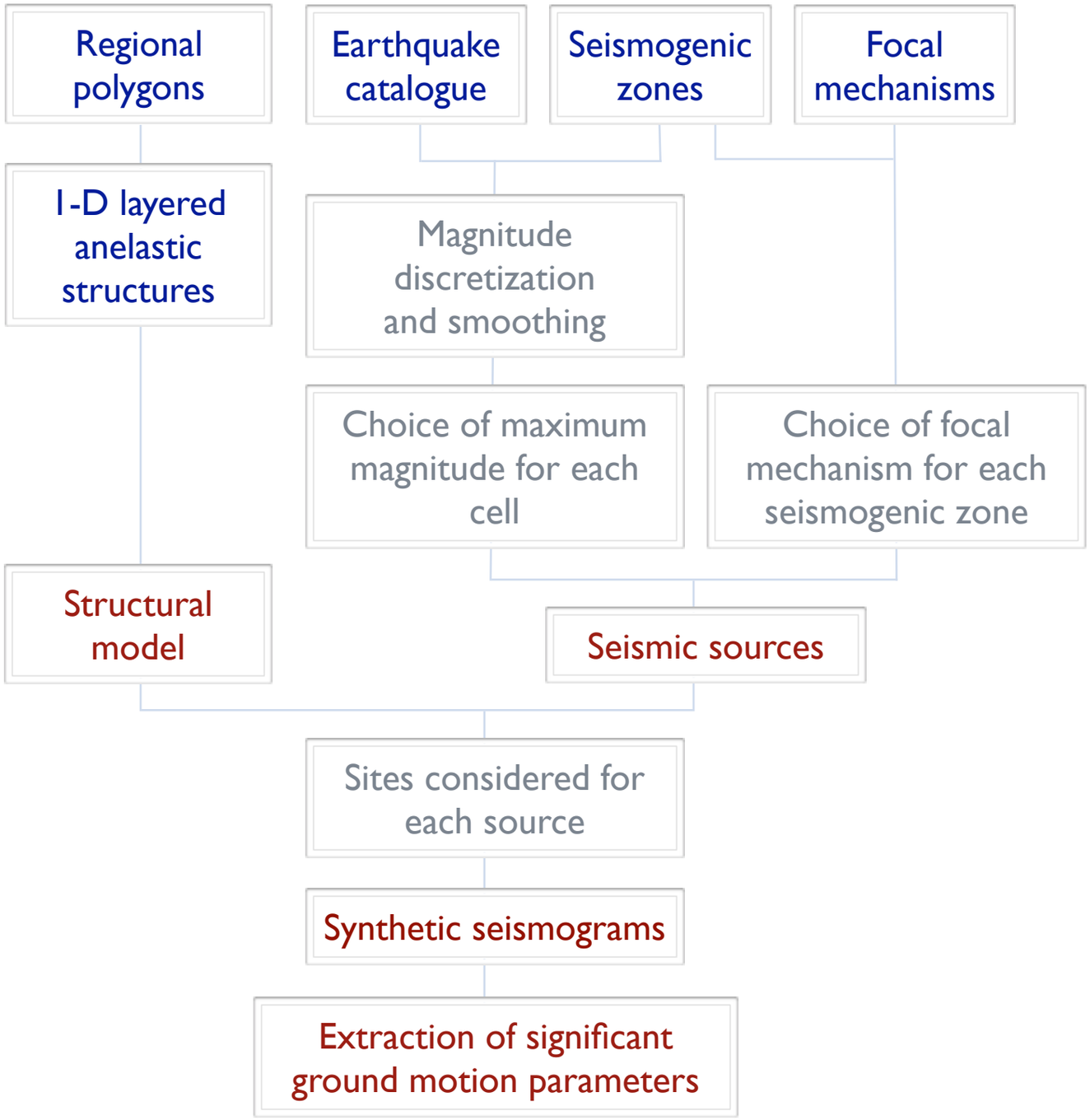

- Seismic zonation based on the computation of synthetic seismograms on the nodes of a grid that covers the study area
- Average structural properties
- Simple source model (scaled point source)
- Cut-off frequency 1 Hz
- Maps of peak displacement, velocity and Design Ground Acceleration

Regional Scale - Structural models

Regional polygons

Earthquake catalogue

Seismogenic zones

Focal mechanisms

1-D layered anelastic structures

Magnitude discretization and smoothing

Choice of maximum magnitude for each cell

Choice of focal mechanism for each seismogenic zone

Structural model

Seismic sources

Sites considered for each source

Synthetic seismograms

Extraction of significant ground motion parameters

Regional Scale

Regional polygons

Earthquake catalogue

Seismogenic zones

Focal mechanisms

1-D layered anelastic structures

Magnitude discretization and smoothing

Choice of maximum magnitude for each cell

Choice of focal mechanism for each seismogenic zone

Structural model

Seismic sources

Sites considered for each source

Synthetic seismograms

Extraction of significant ground motion parameters

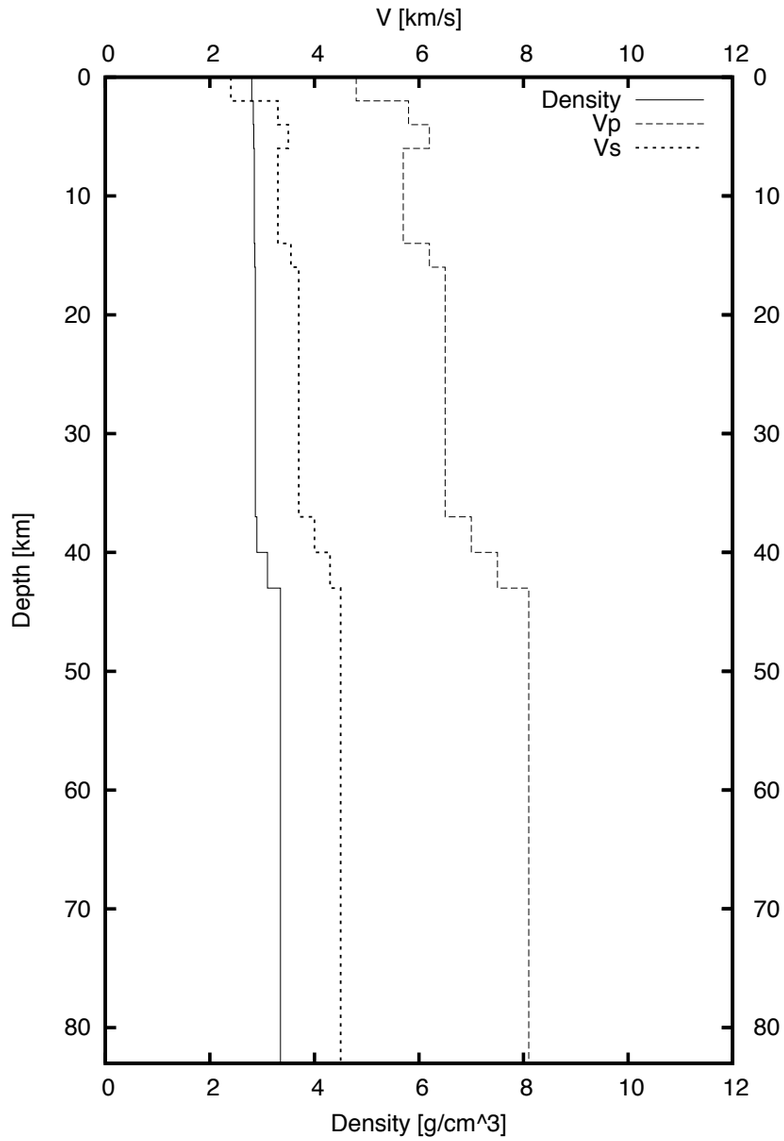

Regional Scale - Historical seismicity

Regional polygons

Earthquake catalogue

Seismogenic zones

Focal mechanisms

1-D layered anelastic structures

Magnitude discretization and smoothing

Choice of maximum magnitude for each cell

Choice of focal mechanism for each seismogenic zone

Structural model

Seismic sources

Sites considered for each source

Synthetic seismograms

Extraction of significant ground motion parameters

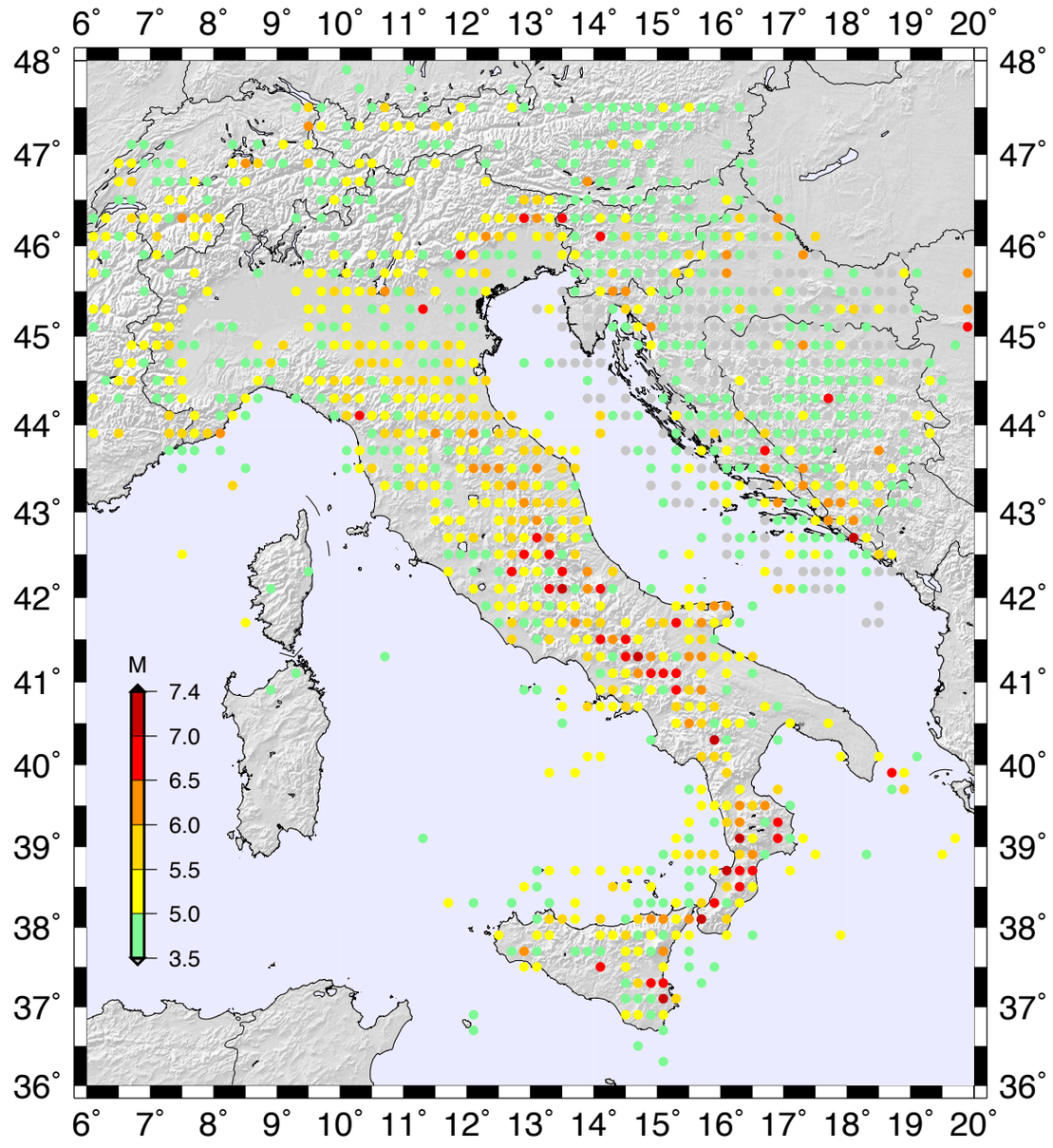

Regional Scale - Tectonic setting

Regional polygons

Earthquake catalogue

Seismogenic zones

Focal mechanisms

1-D layered anelastic structures

Magnitude discretization and smoothing

Choice of maximum magnitude for each cell

Choice of focal mechanism for each seismogenic zone

Structural model

Seismic sources

Sites considered for each source

Synthetic seismograms

Extraction of significant ground motion parameters

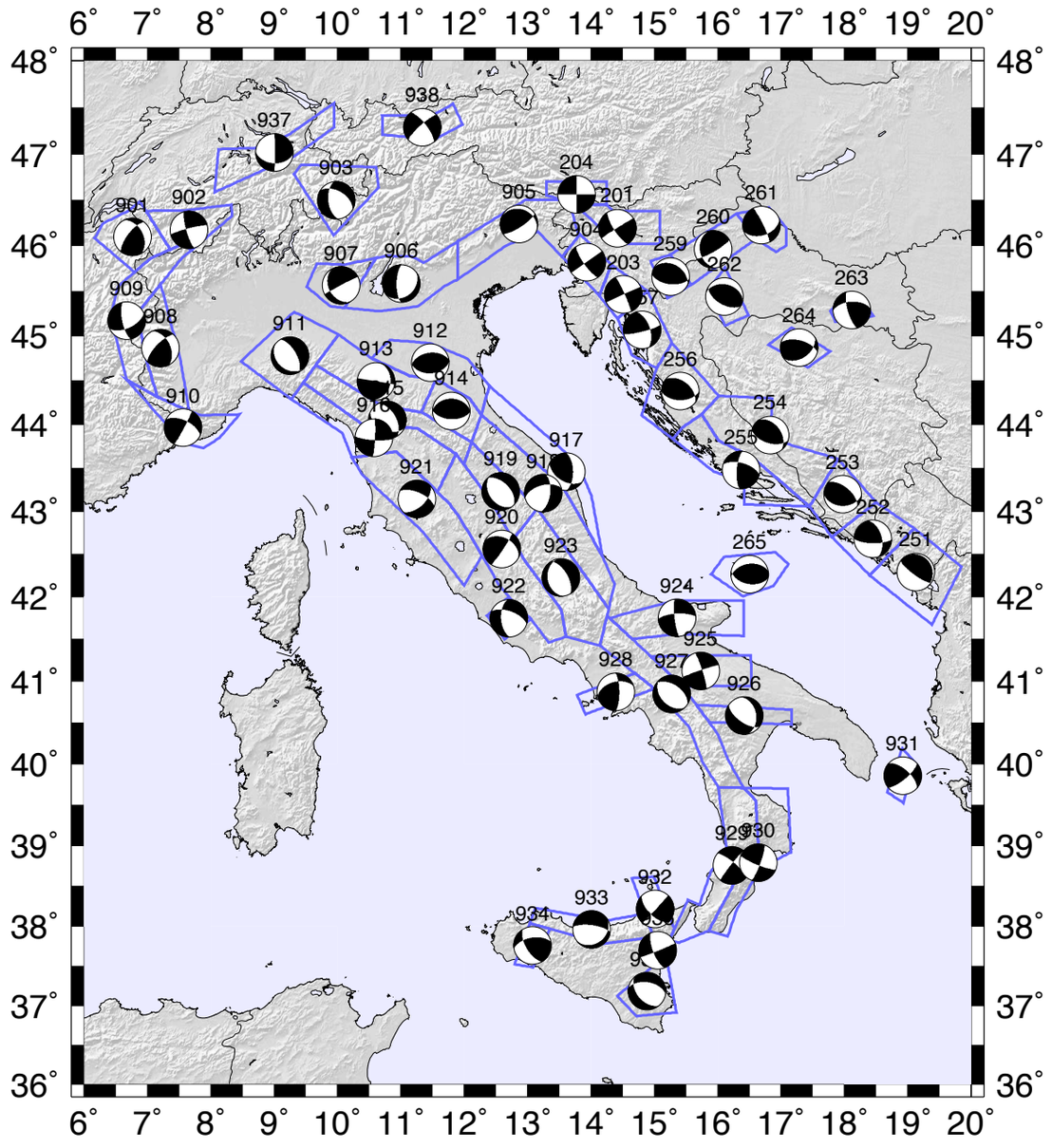

Regional Scale - Seismograms computation

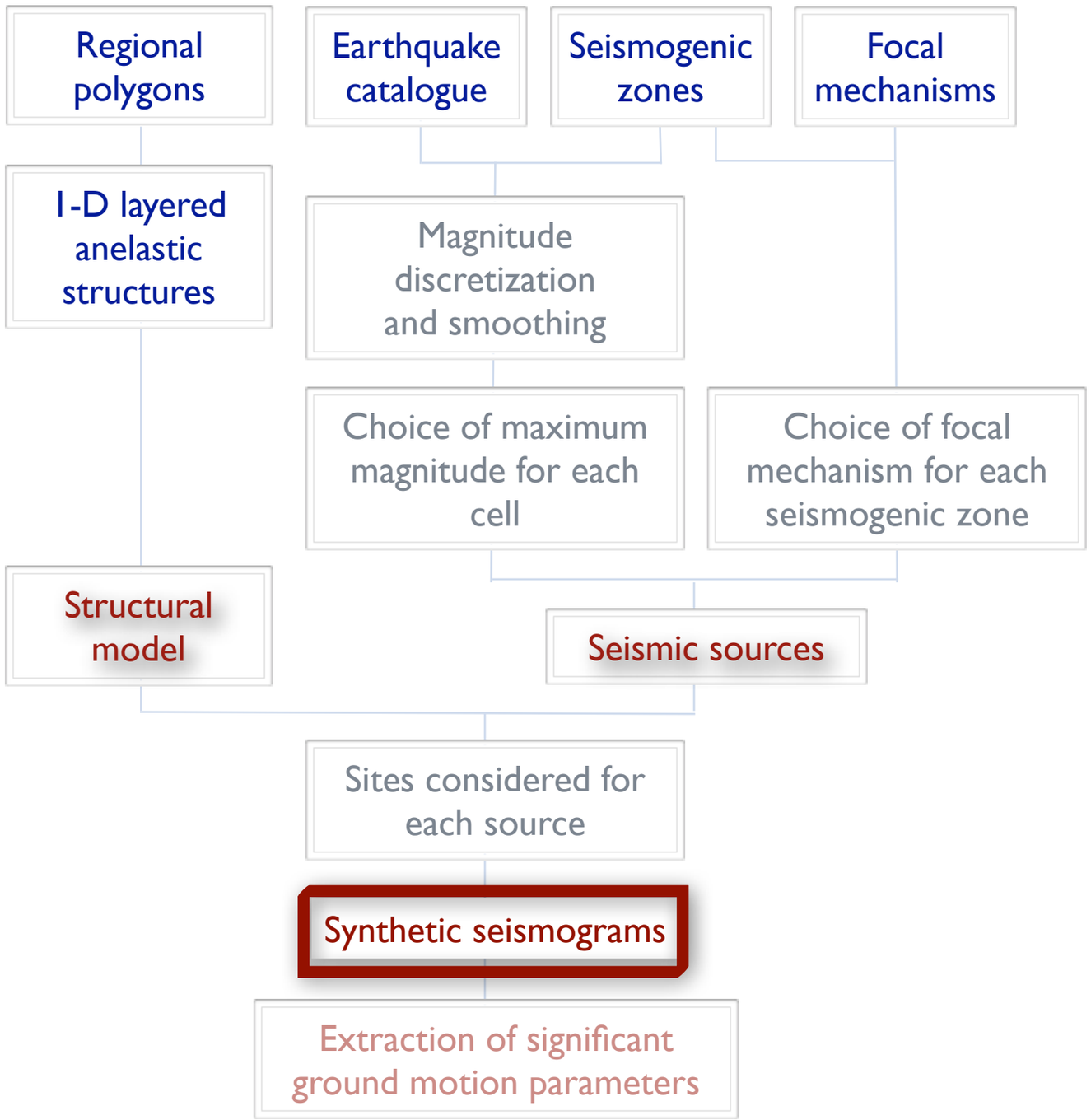

Equivalent Forces

The observable seismic radiation is through energy release as the fault surface moves: formation and propagation of a crack. This complex dynamical problem can be studied by kinematical equivalent approaches.

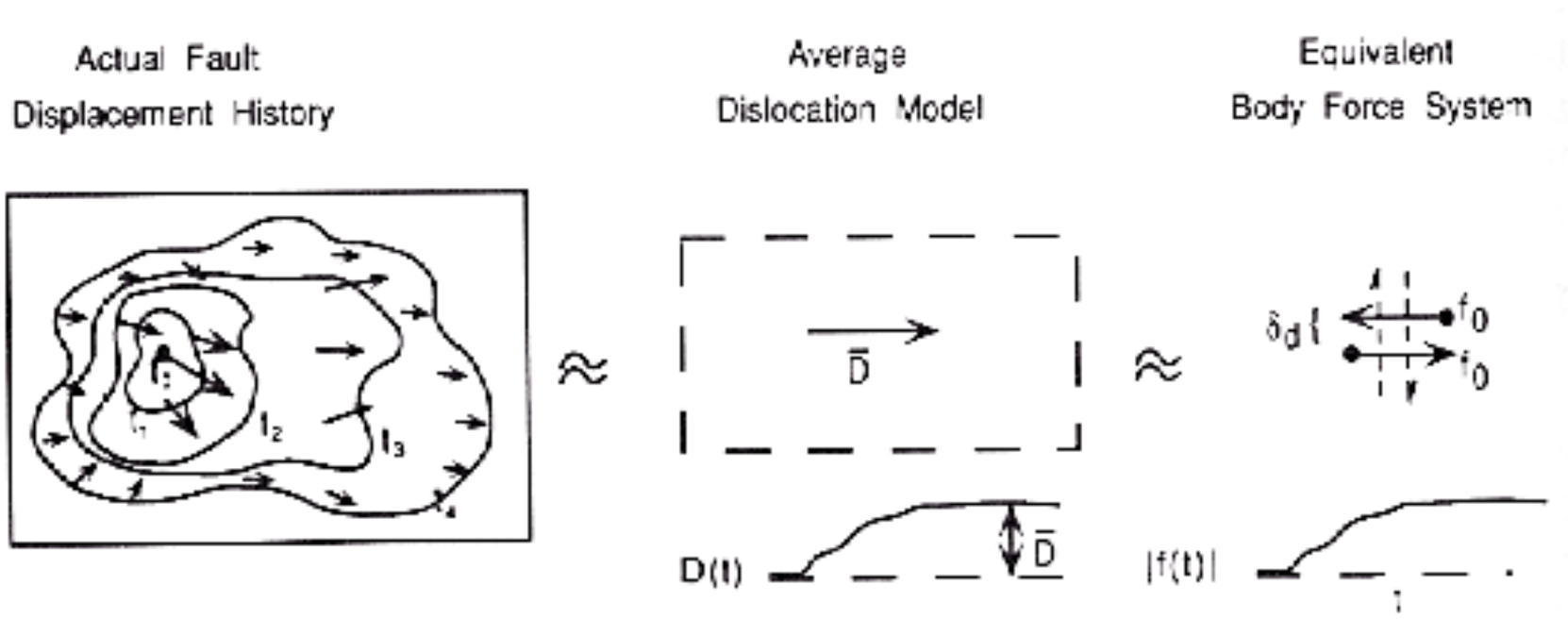

The scope is to develop a representation of the displacement generated in an elastic body in terms of the quantities that originated it: body forces and applied tractions and displacements over the surface of the body.

The actual slip process will be described by superposition of equivalent body forces acting in space (over a fault) and time (rise time).

Final source representation

$$u_n(\mathbf{x},t) = \iint_{\Sigma} [u_i] c_{ijpq} \nu_j * \frac{\partial G_{np}}{\partial \xi_q} d\Sigma$$

$$m_{pq} = [u_i] c_{ijpq} \nu_j \qquad u_n(\mathbf{x},t) = \iint_{\Sigma} m_{pq} * \frac{\partial G_{np}}{\partial \xi_q} d\Sigma$$

And if the source can be considered a point-source (for distances greater than fault dimensions), the contributions from different surface elements can be considered in phase.

Thus for an effective point source, one can define the moment tensor:

$$M_{pq} = \iint_{\Sigma} m_{pq} d\Sigma$$

$$u_n(\mathbf{x},t) = M_{pq} * G_{np,q}$$

GF for double couple

An important case to consider in detail is the radiation pattern expected when the source is a double-couple. The result for a moment time function $M_0(t)$ is:

$$u = \frac{A^{NF}}{4\pi\rho|\mathbf{x}|^4}\int_{|\mathbf{x}|/\alpha}^{|\mathbf{x}|/\beta}\tau M_0(t-\tau)d\tau +$$

$$+\frac{A_P^{IF}}{4\pi\rho\alpha^2|\mathbf{x}|^2}M_0\left(t-\frac{|\mathbf{x}|}{\alpha}\right)-\frac{A_S^{IF}}{4\pi\rho\beta^2|\mathbf{x}|^2}M_0\left(t-\frac{|\mathbf{x}|}{\beta}\right)+$$

$$+\frac{A_P^{FF}}{4\pi\rho\alpha^3|\mathbf{x}|}\dot{M}_0\left(t-\frac{|\mathbf{x}|}{\alpha}\right)-\frac{A_S^{FF}}{4\pi\rho\beta^3|\mathbf{x}|}\dot{M}_0\left(t-\frac{|\mathbf{x}|}{\beta}\right)$$

$$A^{NF} = 9\sin2\theta\cos\phi\hat{\mathbf{r}} - 6\left(\cos2\theta\cos\phi\hat{\boldsymbol{\theta}} - \cos\theta\sin\phi\hat{\boldsymbol{\phi}}\right)$$

Near field term

$$A_P^{IF} = 4\sin2\theta\cos\phi\hat{\mathbf{r}} - 2\left(\cos2\theta\cos\phi\hat{\boldsymbol{\theta}} - \cos\theta\sin\phi\hat{\boldsymbol{\phi}}\right)$$

$$A_S^{IF} = -3\sin2\theta\cos\phi\hat{\mathbf{r}} + 3\left(\cos2\theta\cos\phi\hat{\boldsymbol{\theta}} - \cos\theta\sin\phi\hat{\boldsymbol{\phi}}\right)$$

Intermediate field term

$$A_P^{FF} = \sin2\theta\cos\phi\hat{\mathbf{r}}$$

$$A_S^{FF} = \cos2\theta\cos\phi\hat{\boldsymbol{\theta}} - \cos\theta\sin\phi\hat{\boldsymbol{\phi}}$$

Far field term

NF DC (static) Radiation pattern

The static final displacement for a shear dislocation of strength M_0 is:

$$u = \frac{M_0(\infty)}{4\pi\rho|\mathbf{x}|^2}\left[A^{NF}\left(\frac{1}{2\beta^2}-\frac{1}{2\alpha^2}\right)+\frac{A_P^{IF}}{\alpha^2}+\frac{A_S^{IF}}{\beta^2}\right]=$$

$$=\frac{M_0(\infty)}{4\pi\rho|\mathbf{x}|^2}\left[\left(\frac{3}{2\beta^2}-\frac{1}{2\alpha^2}\right)\sin 2\theta\cos\phi\hat{\mathbf{r}}+\frac{1}{\alpha^2}\left(\cos 2\theta\cos\phi\hat{\boldsymbol{\theta}}-\cos\theta\sin\phi\hat{\boldsymbol{\phi}}\right)\right]$$

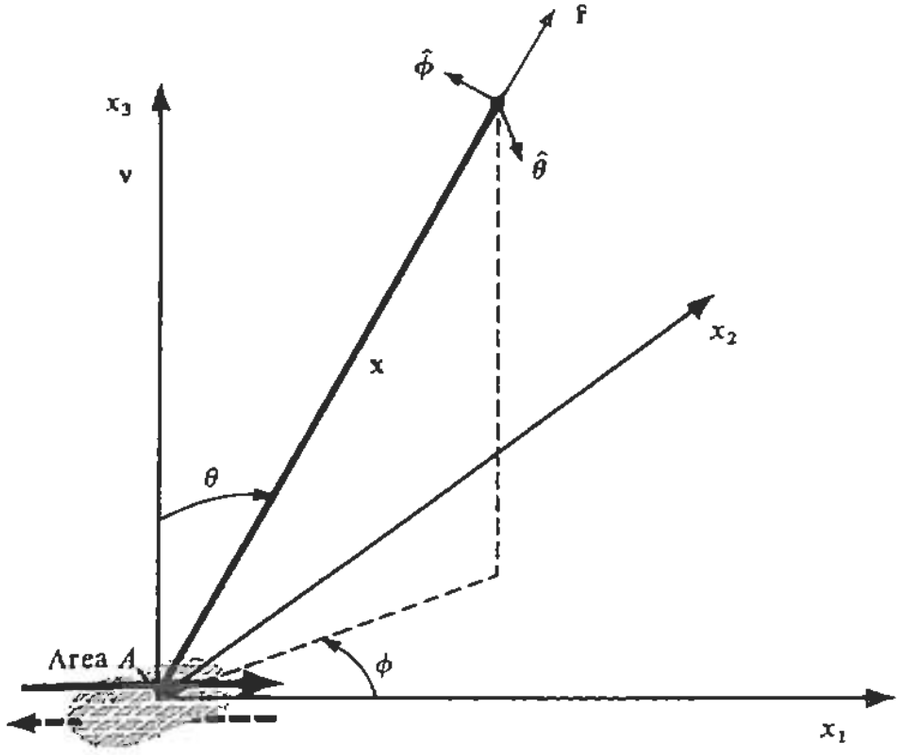

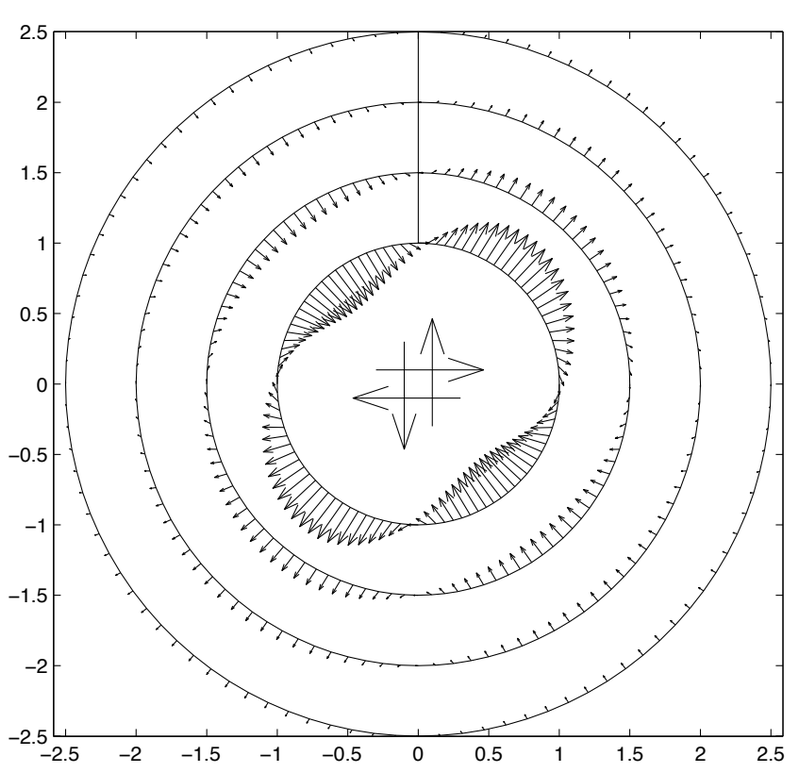

Figure 7: Near-field Static Displacement Field From a Point Double Couple Source ($\phi = 0$ plane); $\alpha = 3^{1/2}$, $\beta = 1$, $r = 0.1,\ 0.15,\ 0.20,\ 0.25$, $\rho = 1/4\pi$, $M_\infty = 1$; self-scaled displacements

Coseismic deformation

L'Aquila (Italy) earthquake, Mw 6.3.
Horizontal and Vertical surface displacement from InSAR Data
(assuming horizontal displacement is perpendicular to the fault strike ~N48W).

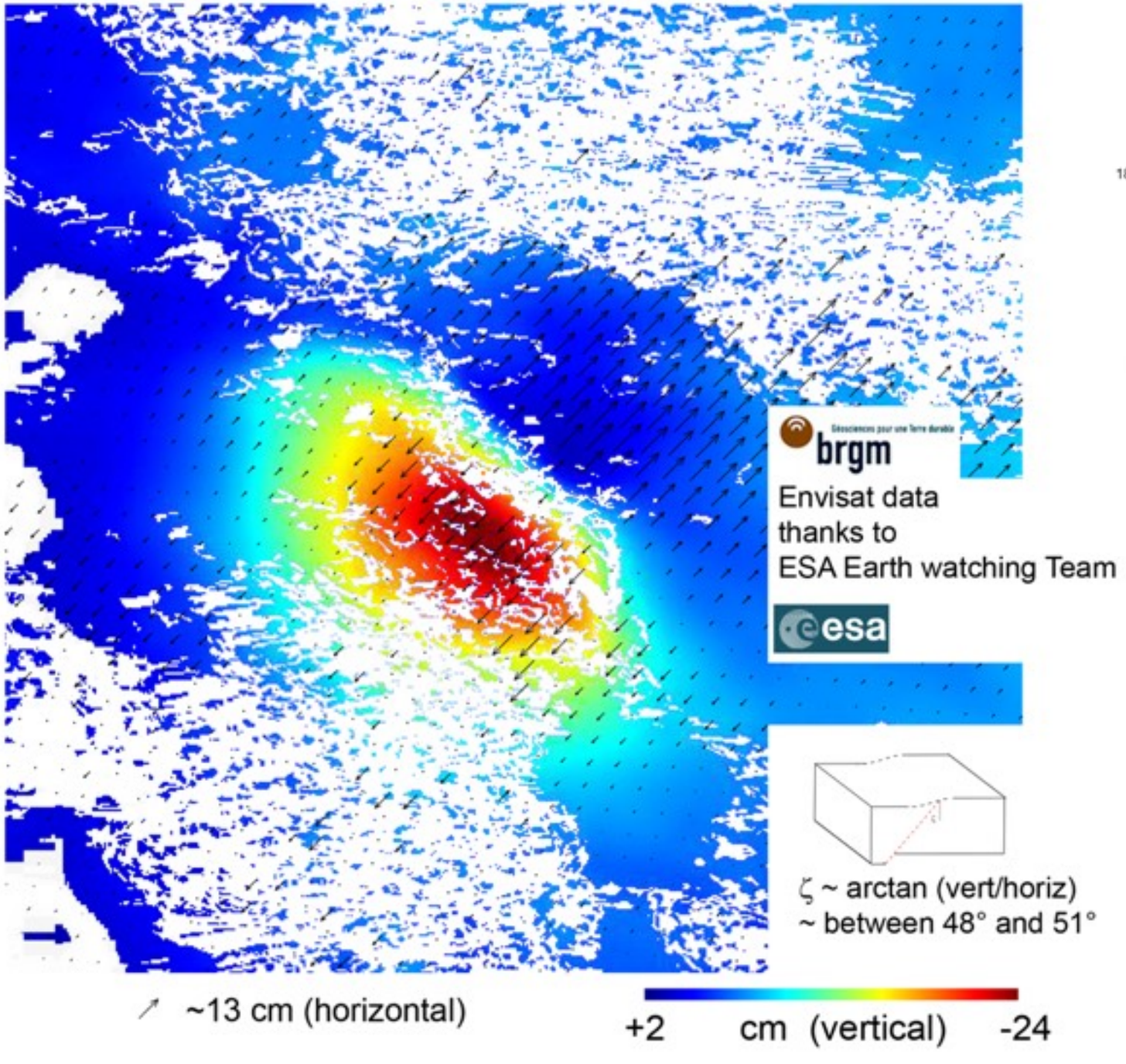

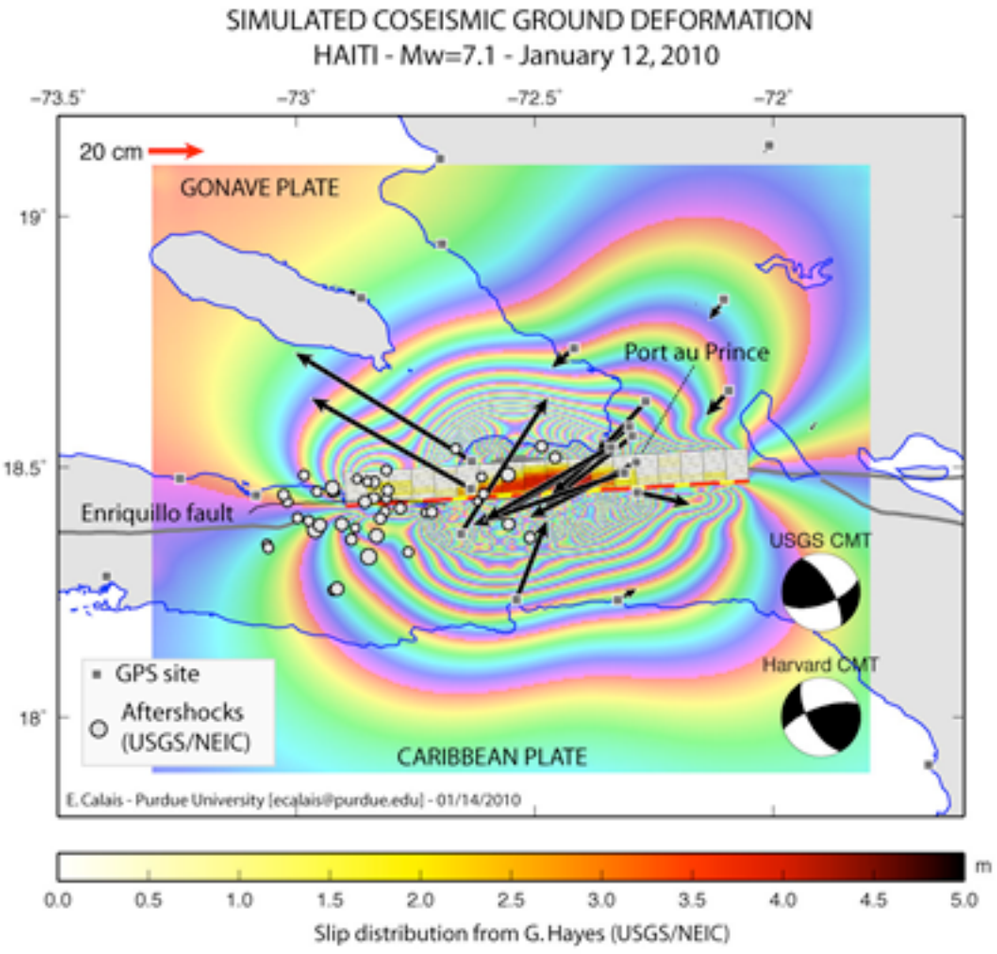

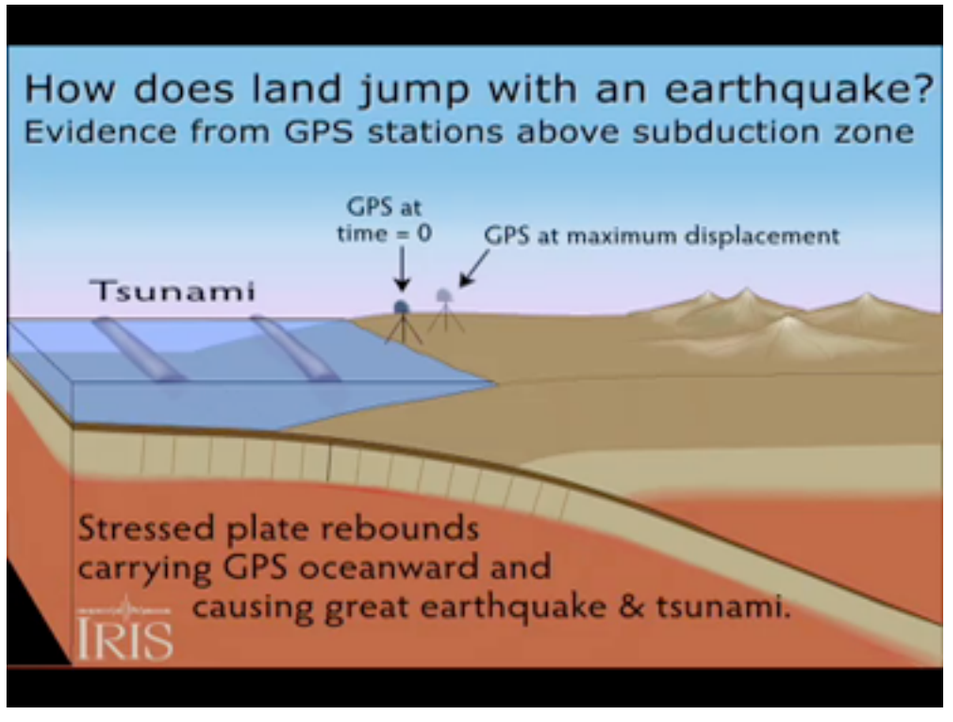

Co- & Post- seismic: Tohoku-oki

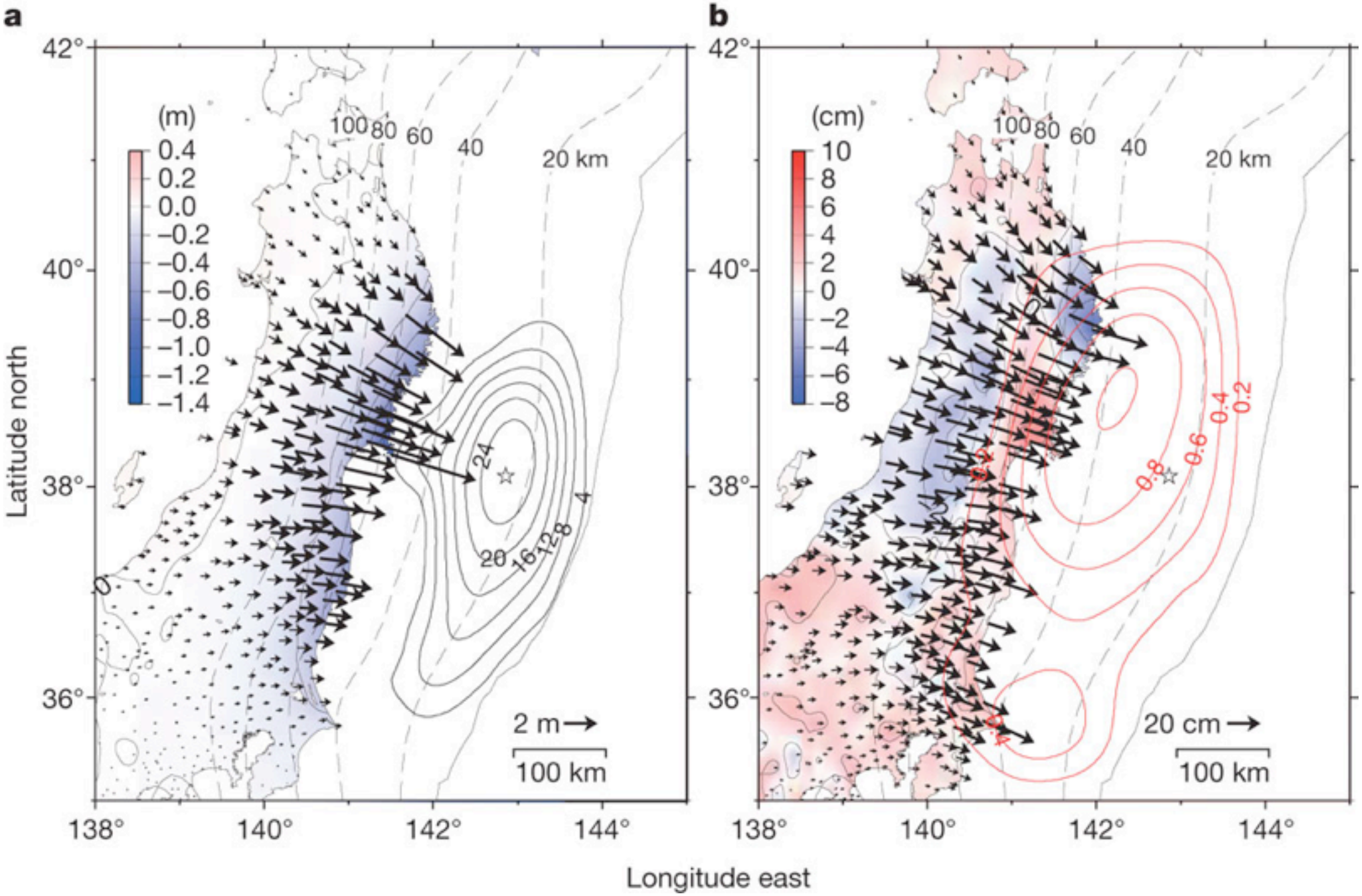

a, Coseismic displacements for 10–11 March 2011, relative to the Fukue site. The black arrows indicate the horizontal coseismic movements of the GPS sites. The colour shading indicates vertical displacement. The star marks the location of the earthquake epicentre. The dotted lines indicate the isodepth contours of the plate boundary at 20-km intervals28. The solid contours show the coseismic slip distribution in metres.
b, Postseismic displacements for 12–25 March 2011, relative to the Fukue site. The red contours show the afterslip distribution in metres. All other markings represent the same as in a.

From: Ozawa et al., 2011,, Nature, 475, 373–376.

Far field for a point d-c point source

From the representation theorem we have:

$$u_n(\mathbf{x},t) = M_{pq} * G_{np,q}$$

that, in the far field and in a spherical coordinate system becomes:

$$\mathbf{u}(\mathbf{x},t) = \frac{1}{4\pi\rho\alpha^3}\left(\sin 2\theta\cos\phi\hat{\mathbf{r}}\right)\frac{\dot{M}(t-r/\alpha)}{r} +$$

$$\frac{1}{4\pi\rho\beta^3}\left(\cos 2\theta\cos\phi\hat{\boldsymbol{\theta}} - \cos\theta\sin\phi\hat{\boldsymbol{\phi}}\right)\frac{\dot{M}(t-r/\beta)}{r}$$

and both P and S radiation fields are proportional to the time derivative of the moment function (moment rate). If the moment function is a ramp of duration τ (**rise time**), the propagating disturbance in the far-field will be a **boxcar,** with the same duration, and whose amplitude is varying depending on the radiation pattern.

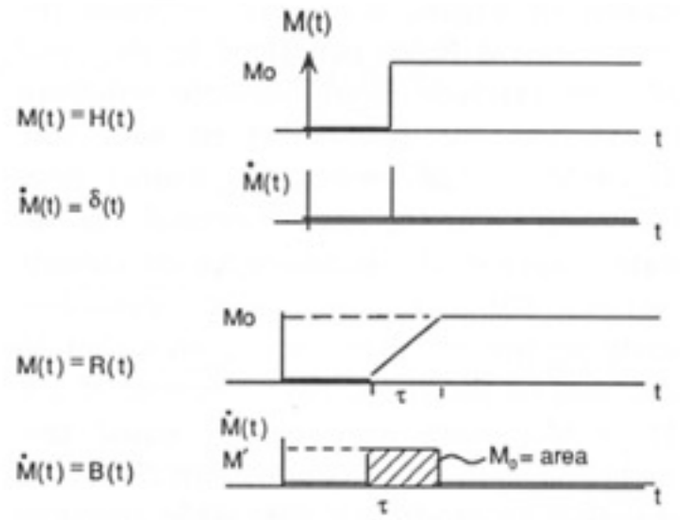

FIGURE 8.21 Far-field *P*- and *S*-wave displacements are proportional to $\dot{M}(t)$, the time derivative of the moment function $M(t) = \mu A(t)D(t)$. Simple step and ramp moment functions generate far-field impulses or boxcar ground motions.

FF DC Radiation pattern

FIGURE **4.5**
Diagrams for the radiation pattern of the radial component of displacement due to a double couple, i.e., $\sin 2\theta \cos\phi\, \hat{\mathbf{r}}$. (**a**) The lobes are a locus of points having a distance from the origin that is proportional to $\sin 2\theta$. The diagram is for a plane of constant azimuth, and the pair of arrows at the center denotes the shear dislocation. Note the alternating quadrants of inward and outward directions. In terms of far-field P-wave displacement, plus signs denote outward displacement (if $\dot{M}_0(t - r/\alpha)$ is positive), and minus signs denote inward displacement. (**b**) View of the radiatiou pattern over a sphere centered on the origin. Plus and minus signs of various sizes denote variation (with θ, ϕ) of outward and inward motions. The fault plane and the auxiliary plane are nodal liues (on which $\sin 2\theta \cos\phi = 0$). An equal-area projection has been used (see Fig. 4.17). Point P marks the pressure axis, and T the tension axis.

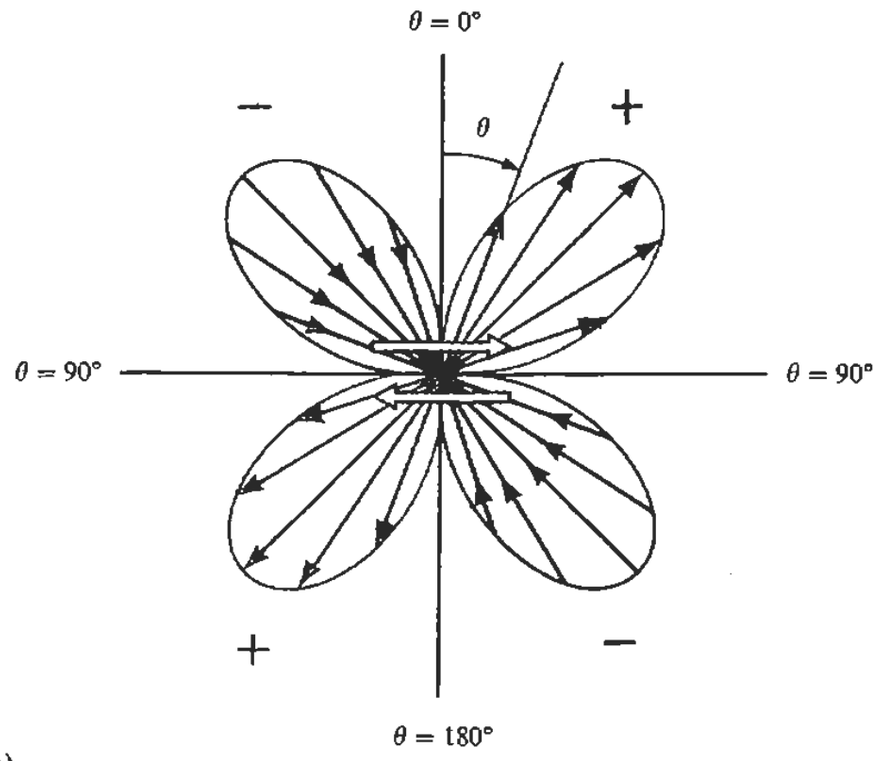

(a)

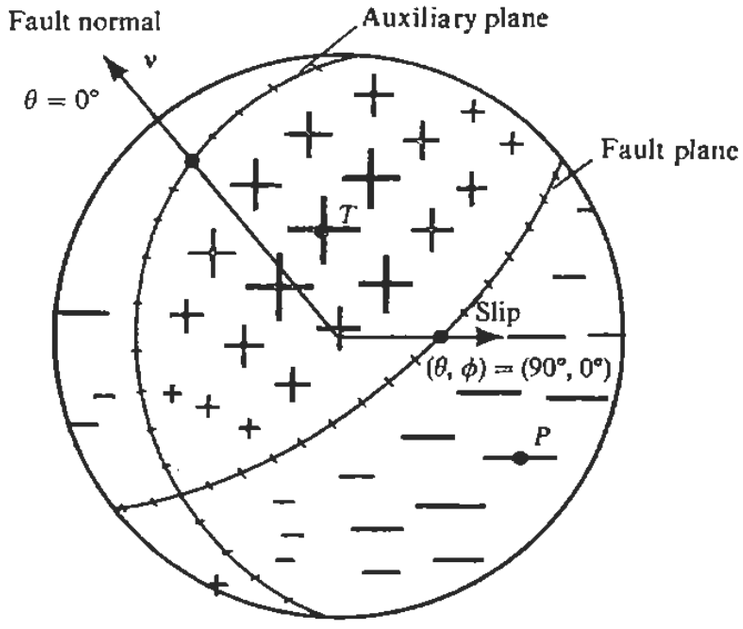

(b)

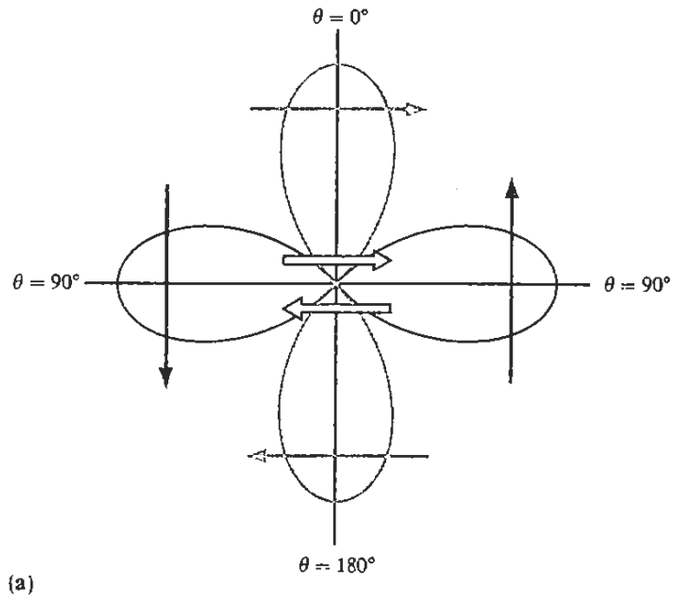

(a)

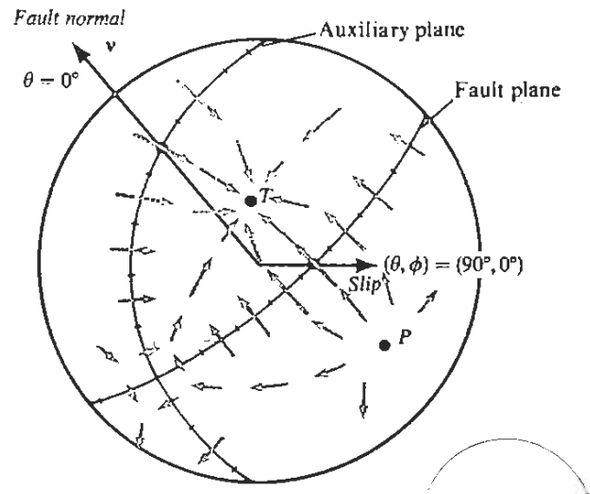

(b)

FIGURE **4.6**
Diagrams for the radiation pattern of the transverse component of displacement due to a double couple, i.e., $\cos 2\theta \cos\phi\, \hat{\theta} - \cos\theta \sin\phi\, \hat{\phi}$. (**a**) The four-lobed pattern in plane $\{\phi = 0, \phi = \pi\}$. The central pair of arrows shows the sense of shear dislocation, and arrows imposed on each lobe show the direction of particle displacement associated with the lobe. If applied to the far-field S-wave displacement, it is assumed that $\dot{M}_0(t - r/\beta)$ is positive. (**b**) Off the two planes $\theta = \pi/2$ and $\{\phi = 0, \phi = \pi\}$, the $\hat{\phi}$ component is nonzero, hence (a) is of limited use. This diagram is a view of the radiation pattern over a whole sphere centered on the origin, and arrows (with varying size and direction) in the spherical surface denote the variation (with θ, ϕ) of the transverse motions. There are no nodal lines (where there is zero motion), but nodal points do occur. Note that the nodal point for transverse motion at $(\theta, \phi) = (45°, 0)$ is a maximum in the radiation pattern for longitudinal motion (Fig. 4.5b). But the maximum transverse motion (e.g., at $\theta = 0$) occurs on a nodal line for the longitudinal motion. The stereographic projection has been used (see Fig. 4.16). It is a conformal projection, meaning that it preserves the angles at which curves intersect and the shapes of small regions, but it does not preserve relative areas.

Methodology - Modal Summation Technique

- Expression of the displacement generated by a double-couple point source in a flat layered halfspace

$$u_y^L(x,z,\omega) = \sum_{m=1}^{\infty} \frac{e^{-i3\pi/4}}{\sqrt{8\pi\omega}} \frac{e^{-ik_m x}}{\sqrt{x}} \frac{\left(\chi_m^L(h_s,\omega)\right)}{\sqrt{c_m v_m I_m}} \frac{\left(F_y(z,\omega)\right)}{\sqrt{v_m I_m}}$$

$$u_x^R(x,z,\omega) = \sum_{m=1}^{\infty} \frac{e^{-i3\pi/4}}{\sqrt{8\pi\omega}} \frac{e^{-ik_m x}}{\sqrt{x}} \frac{\left(\chi_m^R(h_s,\omega)\right)}{\sqrt{c_m v_m I_m}} \frac{\left(F_x(z,\omega)\right)}{\sqrt{v_m I_m}}$$

$$u_z^R(x,z,\omega) = \sum_{m=1}^{\infty} \frac{e^{-i\pi/4}}{\sqrt{8\pi\omega}} \frac{e^{-ik_m x}}{\sqrt{x}} \frac{\left(\chi_m^R(h_s,\omega)\right)}{\sqrt{c_m v_m I_m}} \frac{\left(F_z(z,\omega)\right)}{\sqrt{v_m I_m}}$$

source structure receiver

Methodology - Modal Summation Technique

- Source definition and examples of radiation pattern

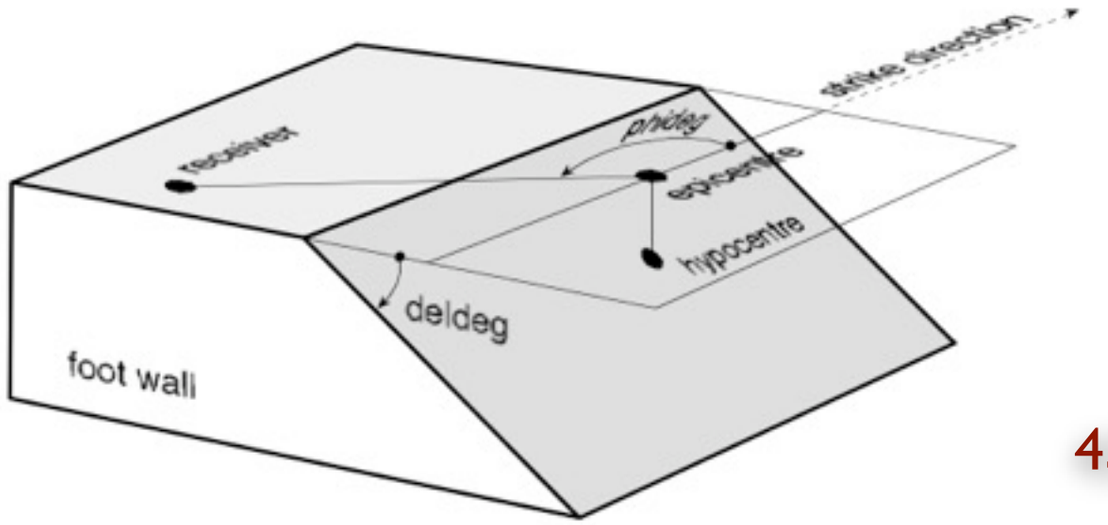

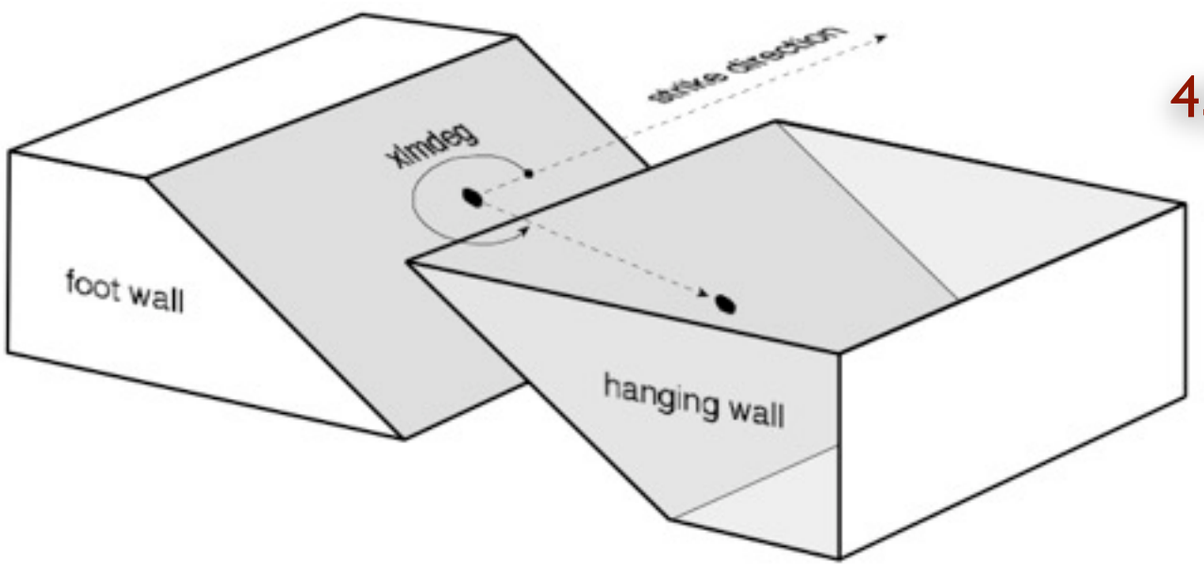

$$\left(\chi_m^L(h_s,\omega)\right) \quad \left(\chi_m^R(h_s,\omega)\right)$$

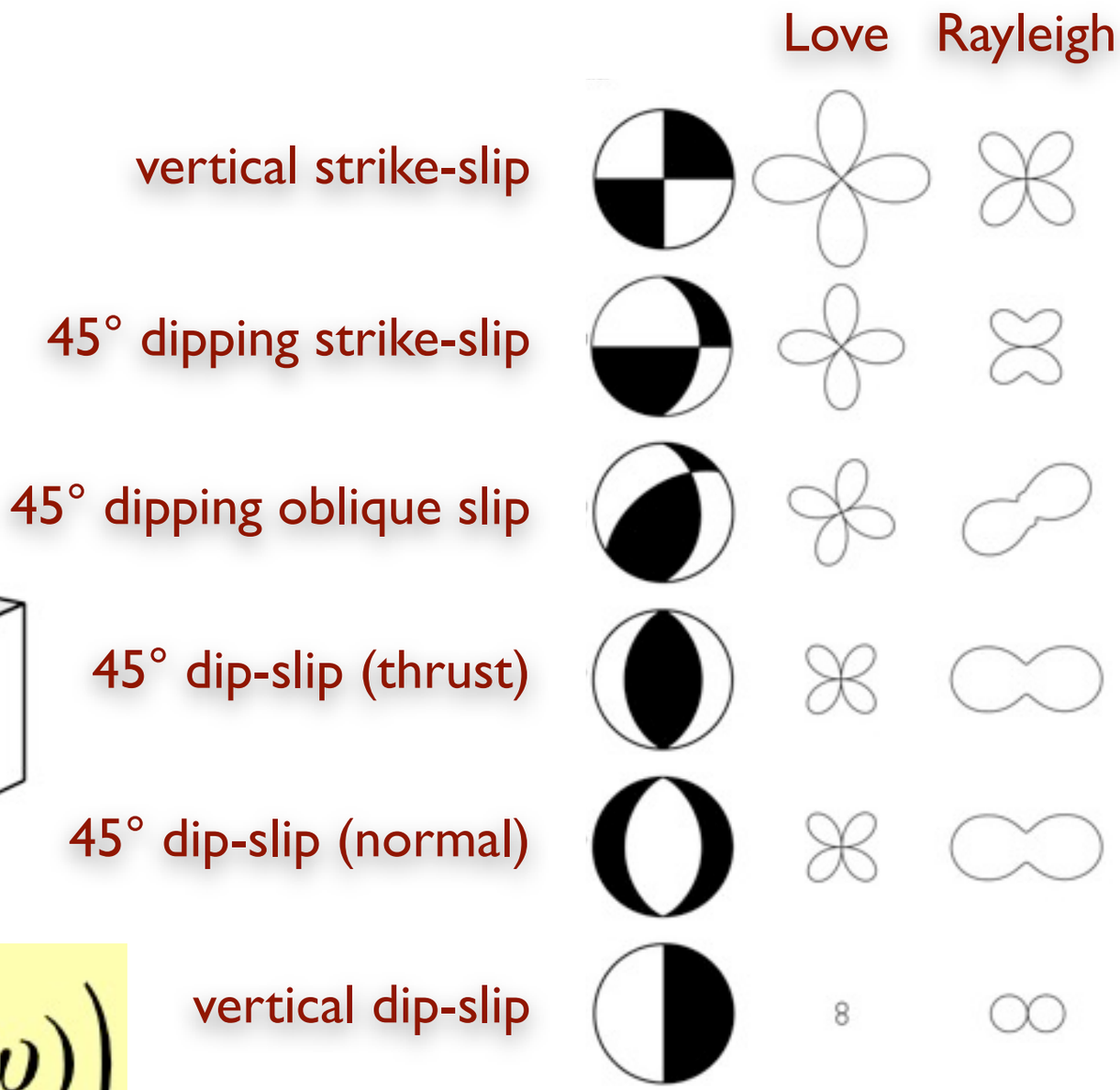

Methodology - Modal Summation Technique

- Expression of the source radiation pattern

$$\chi_L = i(d_{1L}\sin\varphi + d_{2L}\cos\varphi) + d_{3L}\sin 2\varphi + d_{4L}\cos 2\varphi$$

$$\chi_R = d_0 + i(d_{1R}\sin\varphi + d_{2R}\cos\varphi) + d_{3R}\sin 2\varphi + d_{4R}\cos 2\varphi$$

where

$$d_{1L} = G(h_s)\cos\lambda\sin\delta \qquad d_0 = \frac{1}{2}B(h_s)\sin\lambda\sin 2\delta$$

$$d_{2L} = -G(h_s)\sin\lambda\cos 2\delta \qquad d_{1R} = -C(h_s)\sin\lambda\cos 2\delta$$

$$d_{3L} = \frac{1}{2}V(h_s)\sin\lambda\sin 2\delta \qquad d_{2R} = -C(h_s)\cos\lambda\cos\delta$$

$$d_{4L} = V(h_s)\cos\lambda\sin\delta \qquad d_{3R} = A(h_s)\cos\lambda\sin\delta$$

$$d_{4R} = -\frac{1}{2}A(h_s)\sin\lambda\sin 2\delta$$

$$A(h_s) = -\frac{F_x^*(h_s)}{F_z(0)}$$

$$B(h_s) = -\left(3 - 4\frac{\beta^2(h_s)}{\alpha^2(h_s)}\right)\frac{F_x^*(h_s)}{F_z(0)} - \frac{2}{\rho(h_s)\,\alpha^2(h_s)}\frac{\sigma_{zz}^*(h_s)}{\dot{F}_z(0)/c}$$

$$C(h_s) = -\frac{1}{\mu(h_s)}\frac{\sigma_{zx}(h_s)}{\dot{F}_z(0)/c}$$

$$G(h_s) = -\frac{1}{\mu(h_s)}\frac{\sigma_{zy}^*(h_s)}{\dot{F}_y(0)/c}$$

$$V(h_s) = \frac{\dot{F}_y(h_s)}{\dot{F}_y(0)/c} = \frac{F_y(h_s)}{F_y(0)/c}$$

$$\left(\chi_m^L(h_s,\omega)\right) \qquad \left(\chi_m^R(h_s,\omega)\right)$$

Methodology - Modal Summation Technique

- Example of quantities associated with a structure

$$\sqrt{c_m v_m I_m} \qquad \sqrt{v_m I_m}$$

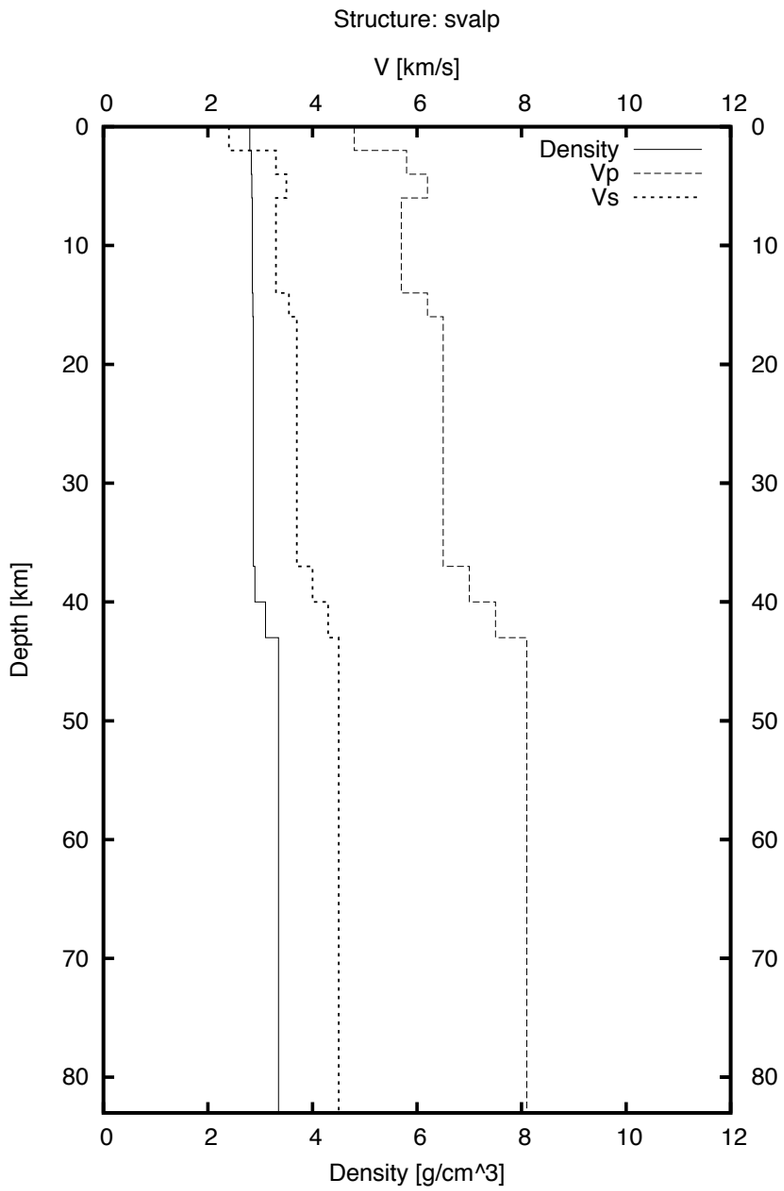

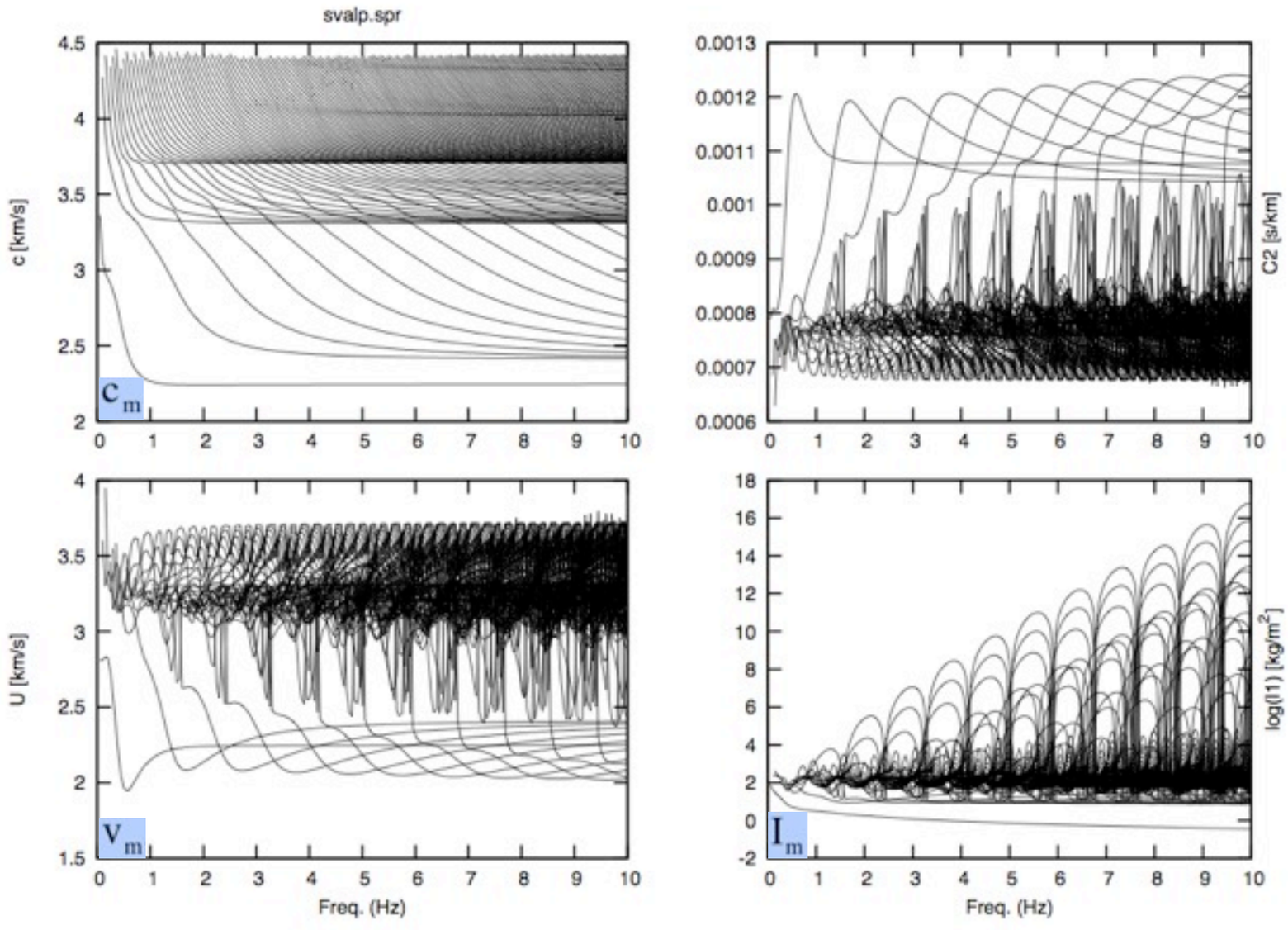

Methodology - Modal Summation Technique

- Phase velocity dispersion curve

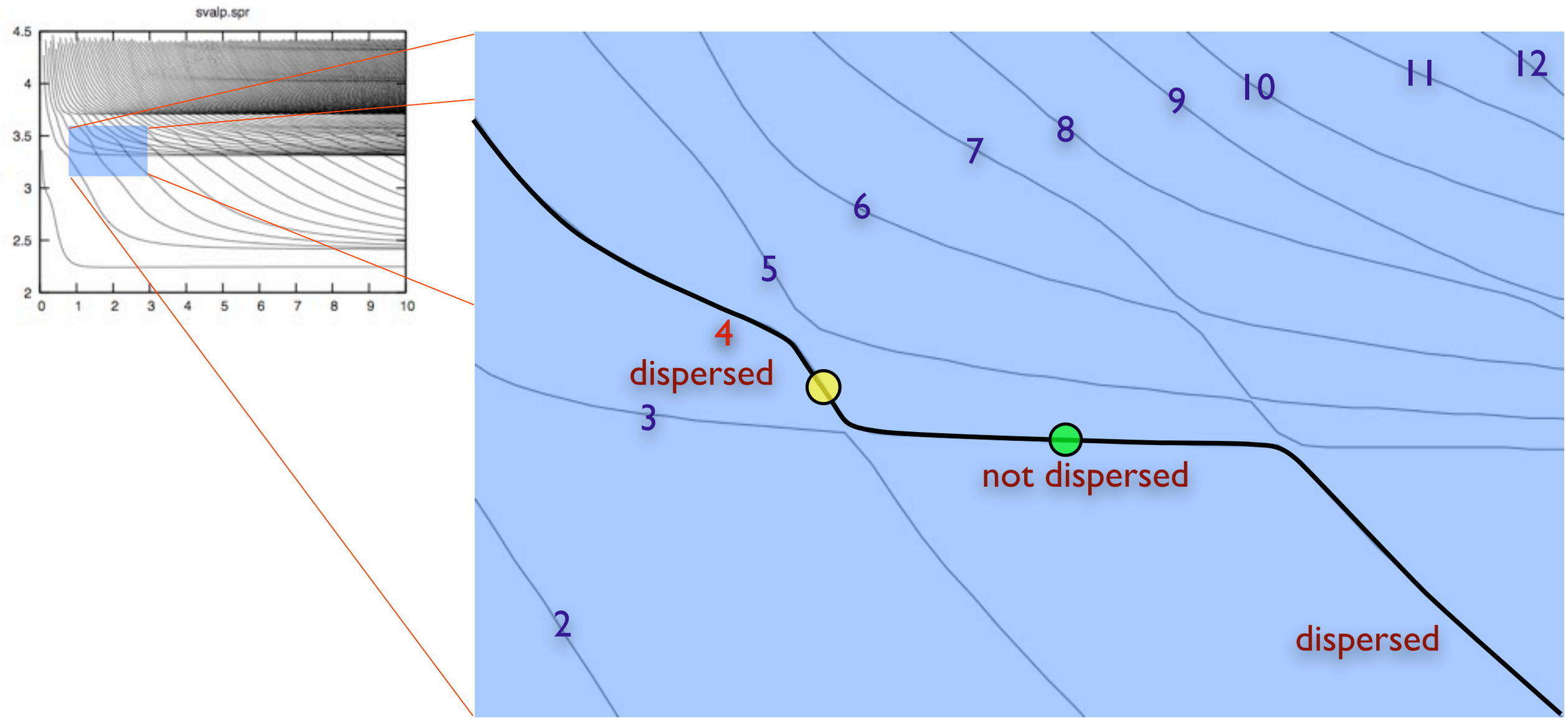

Methodology - Modal Summation Technique

Eigenfunctions

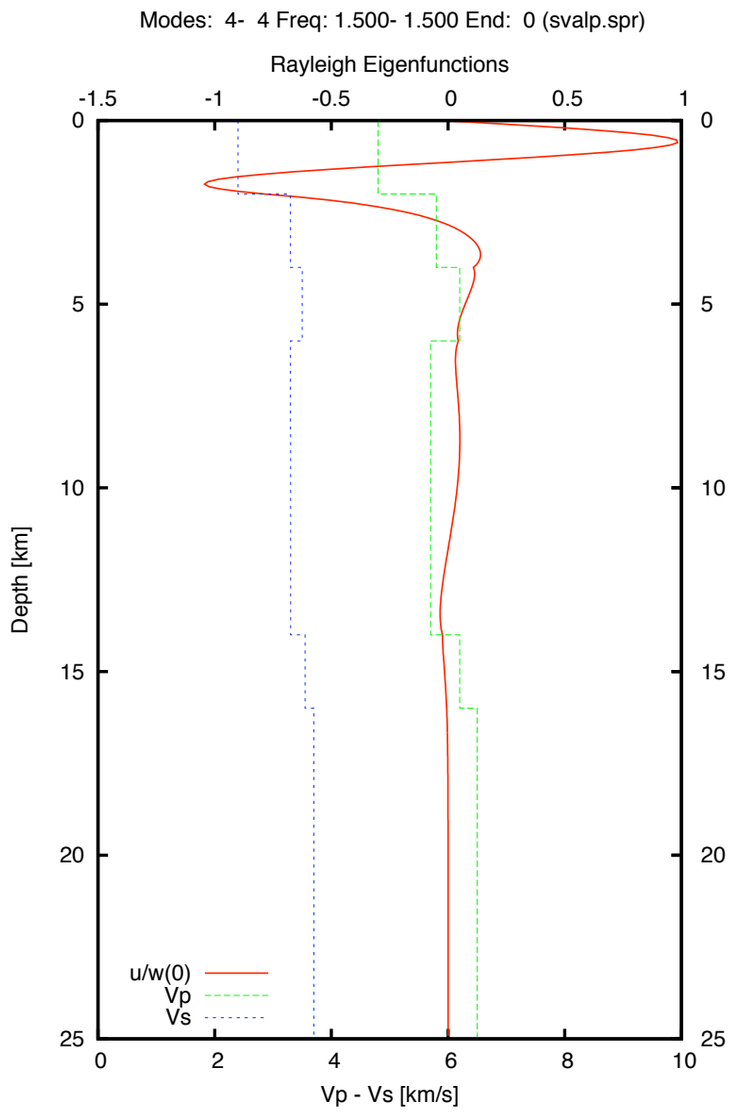

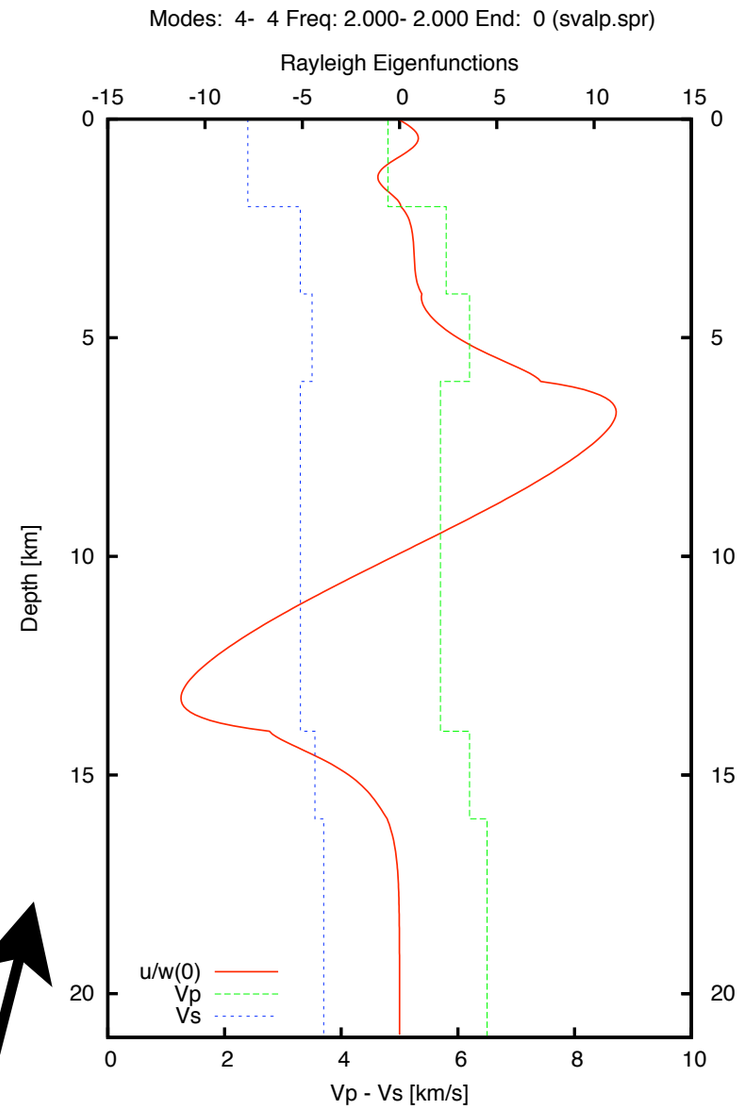

4 dispersed

not dispersed

dispersed

Methodology - Modal Summation Technique

- Synthetic seismograms

$$u_y^L(x,z,\omega) = \sum_{m=1}^{\infty} \frac{e^{-i3\pi/4}}{\sqrt{8\pi\omega}} \frac{e^{-ik_m x}}{\sqrt{x}} \frac{\left(\chi_m^L(h_s,\omega)\right)}{\sqrt{c_m v_m I_m}} \frac{\left(F_y(z,\omega)\right)}{\sqrt{v_m I_m}}$$

$$u_x^R(x,z,\omega) = \sum_{m=1}^{\infty} \frac{e^{-i3\pi/4}}{\sqrt{8\pi\omega}} \frac{e^{-ik_m x}}{\sqrt{x}} \frac{\left(\chi_m^R(h_s,\omega)\right)}{\sqrt{c_m v_m I_m}} \frac{\left(F_x(z,\omega)\right)}{\sqrt{v_m I_m}}$$

$$u_z^R(x,z,\omega) = \sum_{m=1}^{\infty} \frac{e^{-i\pi/4}}{\sqrt{8\pi\omega}} \frac{e^{-ik_m x}}{\sqrt{x}} \frac{\left(\chi_m^R(h_s,\omega)\right)}{\sqrt{c_m v_m I_m}} \frac{\left(F_z(z,\omega)\right)}{\sqrt{v_m I_m}}$$

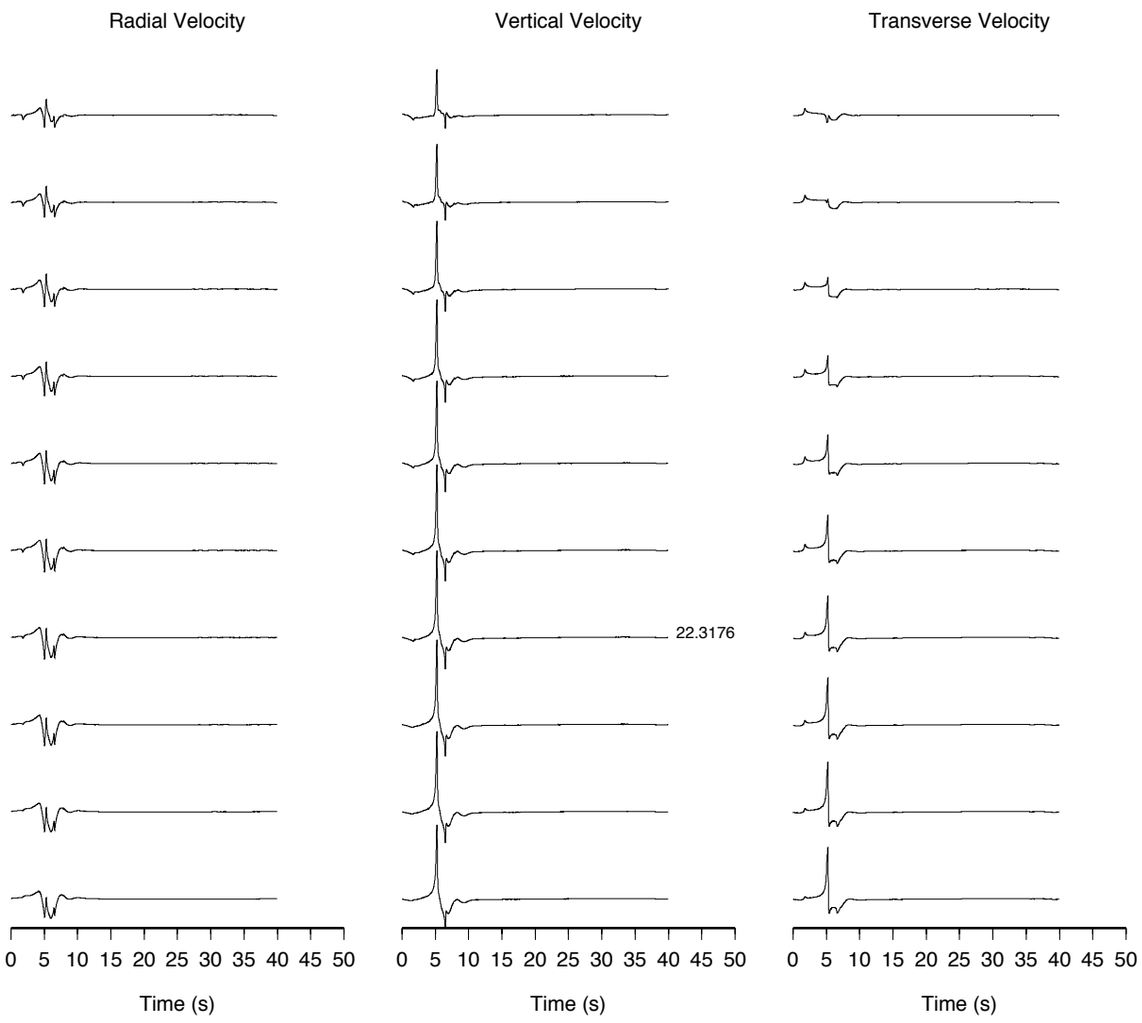

Methodology - Modal Summation Technique

- Synthetic seismograms
- Parametric tests

$$u_y^L(x,z,\omega) = \sum_{m=1}^{\infty} \frac{e^{-i3\pi/4}}{\sqrt{8\pi\omega}} \frac{e^{-ik_m x}}{\sqrt{x}} \frac{\left(\chi_m^L(h_s,\omega)\right)}{\sqrt{c_m v_m I_m}} \frac{\left(F_y(z,\omega)\right)}{\sqrt{v_m I_m}}$$

$$u_x^R(x,z,\omega) = \sum_{m=1}^{\infty} \frac{e^{-i3\pi/4}}{\sqrt{8\pi\omega}} \frac{e^{-ik_m x}}{\sqrt{x}} \frac{\left(\chi_m^R(h_s,\omega)\right)}{\sqrt{c_m v_m I_m}} \frac{\left(F_x(z,\omega)\right)}{\sqrt{v_m I_m}}$$

$$u_z^R(x,z,\omega) = \sum_{m=1}^{\infty} \frac{e^{-i\pi/4}}{\sqrt{8\pi\omega}} \frac{e^{-ik_m x}}{\sqrt{x}} \frac{\left(\chi_m^R(h_s,\omega)\right)}{\sqrt{c_m v_m I_m}} \frac{\left(F_z(z,\omega)\right)}{\sqrt{v_m I_m}}$$

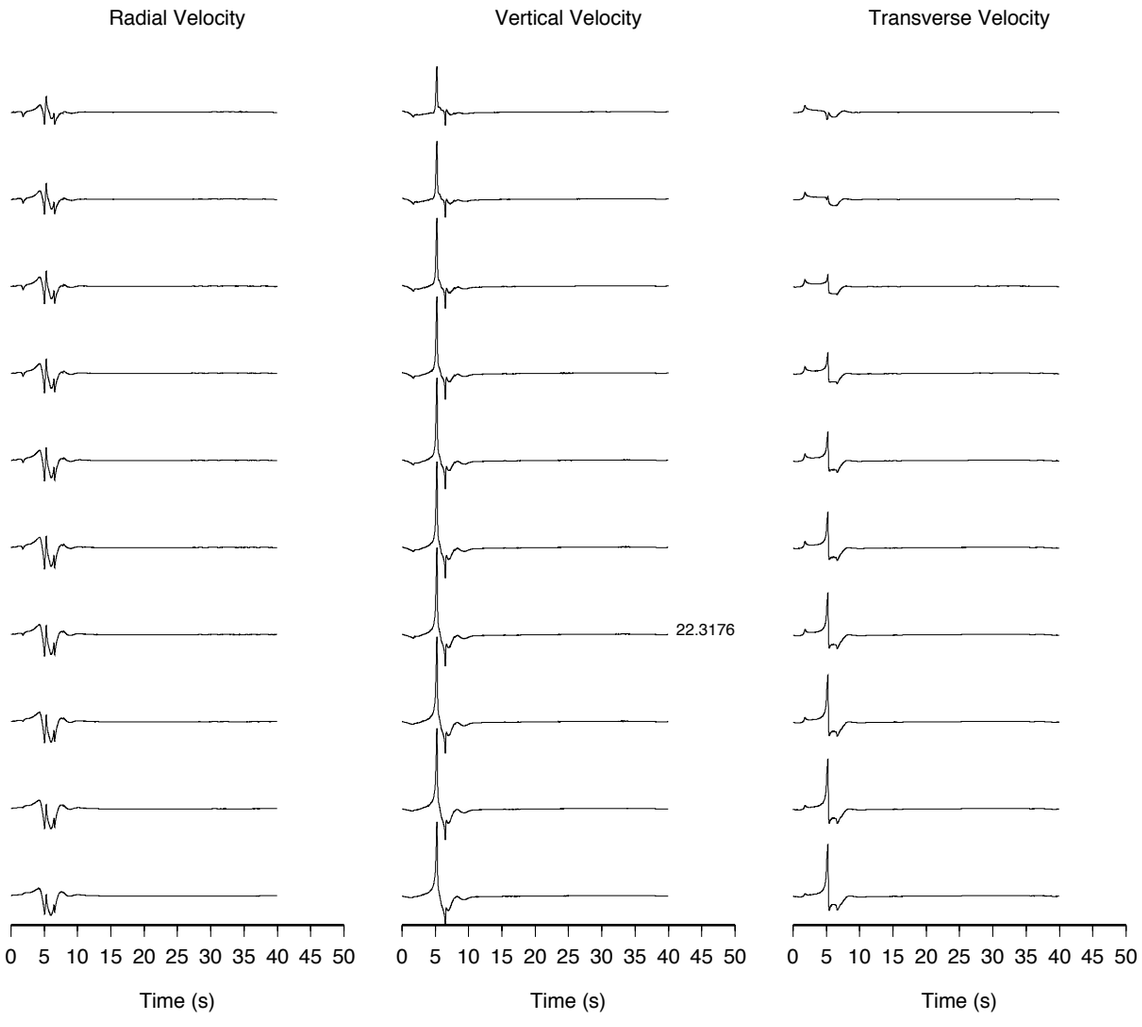

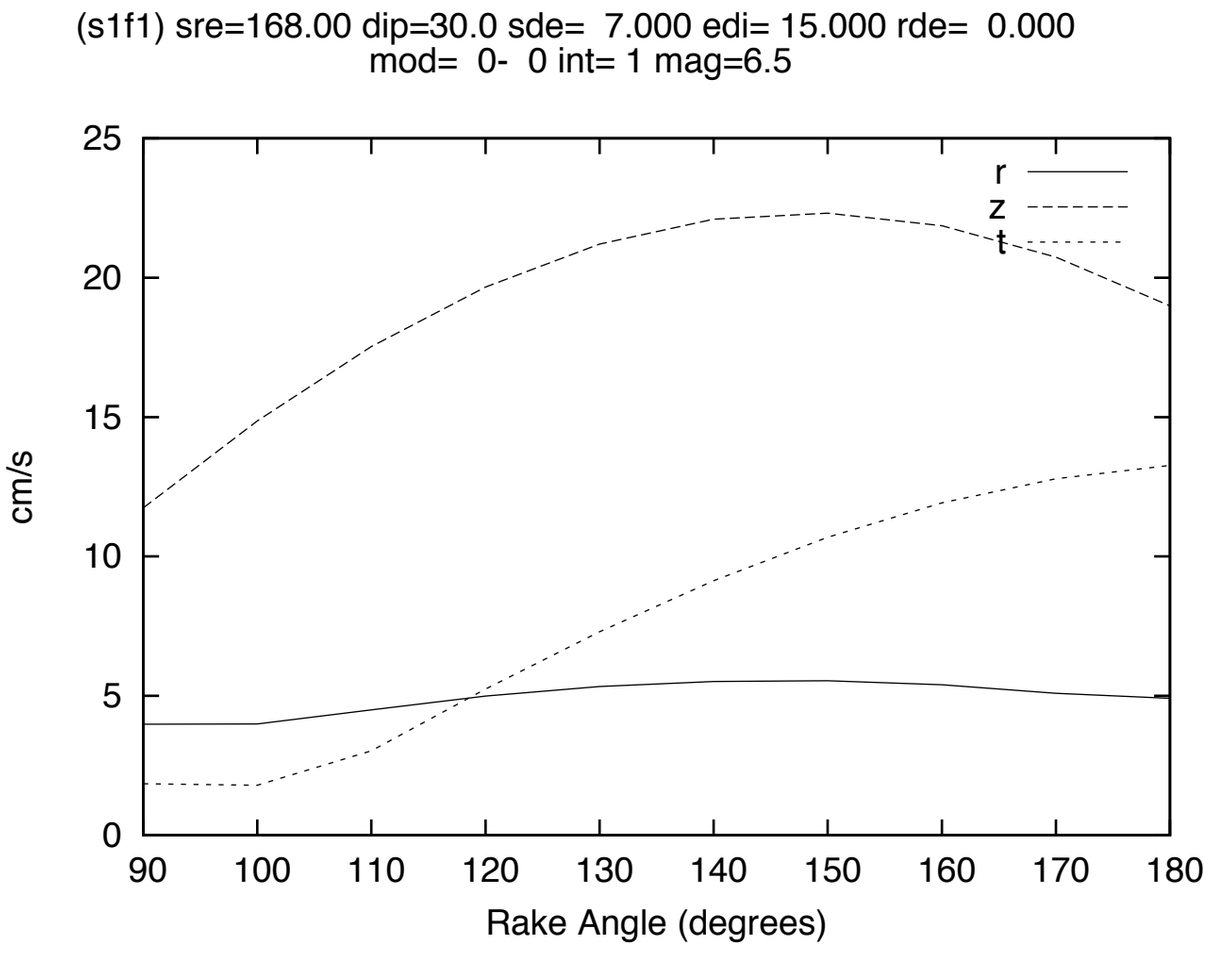

Haskell dislocation model

Haskell N. A. (1964). Total energy spectral density of elastic wave radiation from propagating faults, Bull. Seism. Soc. Am. **54**, 1811–1841

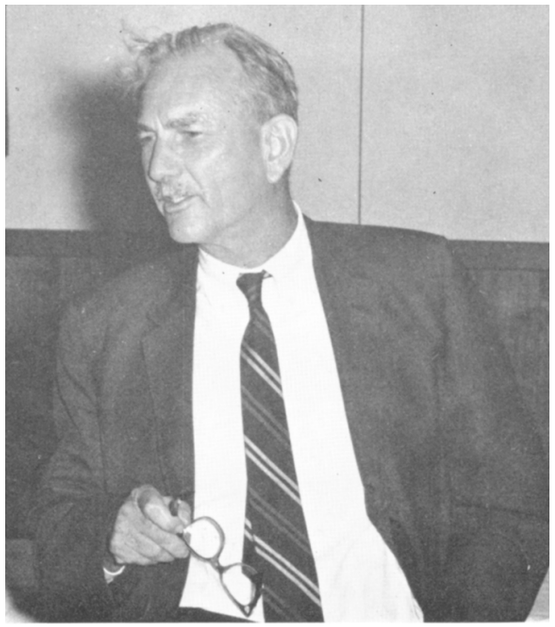

Norman A. Haskell

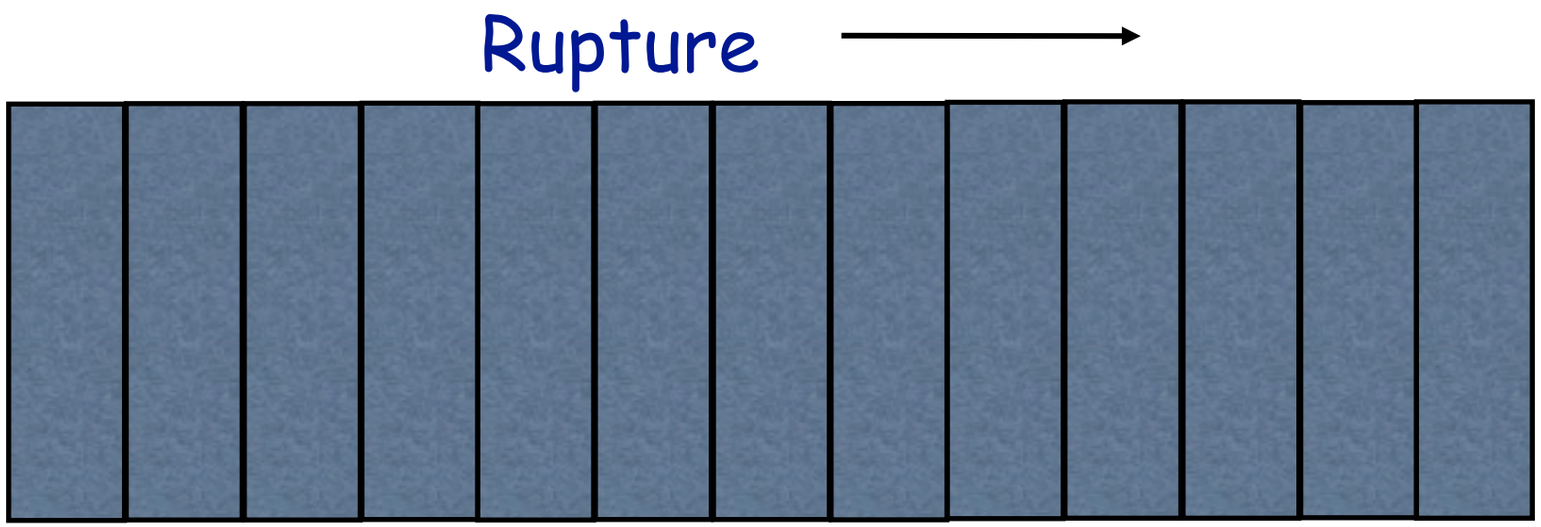

Sumatra earthquake, Dec 28, 2004

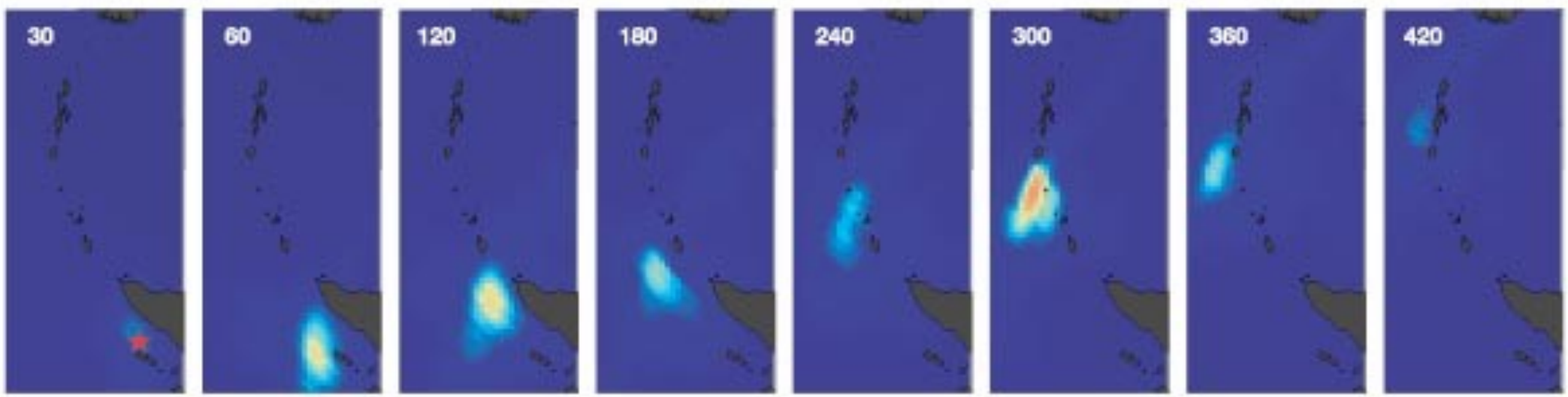

Ishii et al., Nature 2005 doi:10.1038/nature03675

Haskell source model: far field

For a single segment (point source)

$$\mathbf{u}(\mathbf{x},t)=\frac{1}{4\pi\rho\alpha^3}\left(\sin 2\theta\cos\phi\hat{\mathbf{r}}\right)\frac{\dot{M}(t-r/\alpha)}{r}+$$

$$\frac{1}{4\pi\rho\beta^3}\left(\cos 2\theta\cos\phi\hat{\boldsymbol{\theta}}-\cos\theta\sin\phi\hat{\boldsymbol{\phi}}\right)\frac{\dot{M}(t-r/\beta)}{r}$$

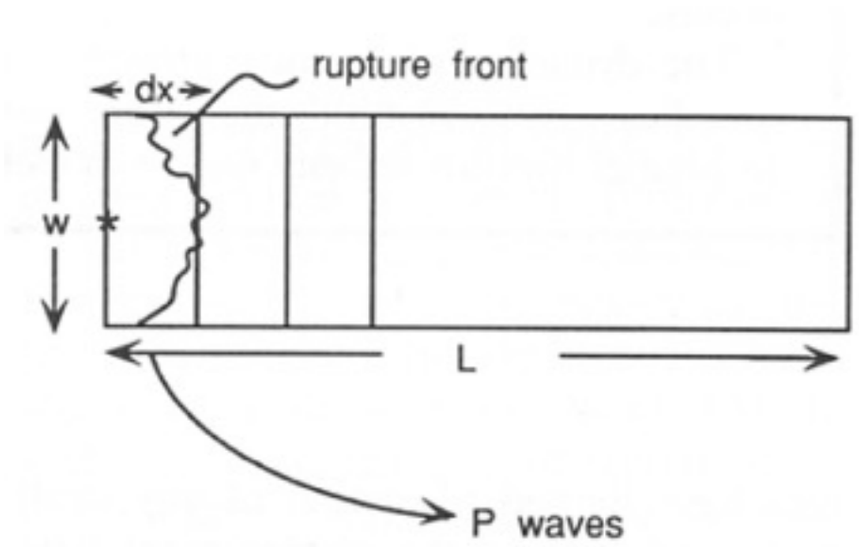

FIGURE 9.5 Geometry of a one-dimensional fault of width *w* and length *L*. The individual segments of the fault are of length *dx*, and the moment of a segment is *m dx*. The fault ruptures with velocity v_r.

$$u_r(r,t)=\sum_{i=1}^{N}u_i\left(r_i,t-r_i/\alpha-\Delta t_i\right)=$$

$$=\frac{R_i^P\mu}{4\pi\rho\alpha^3}W\sum_{i=1}^{N}\frac{\dot{D}_i}{r_i}(t-\Delta t_i)dx\approx$$

$$\approx\frac{R_i^P\mu}{4\pi\rho\alpha^3}\frac{W}{r}\sum_{i=1}^{N}\dot{D}(t)*\delta\left(t-\frac{x}{v_r}\right)dx\approx$$

$$\approx\frac{R_i^P\mu}{4\pi\rho\alpha^3}\frac{W}{r}\dot{D}(t)*\int_0^x\delta\left(t-\frac{x}{v_r}\right)dx=$$

$$=\frac{R_i^P\mu}{4\pi\rho\alpha^3}\frac{W}{r}v_r\dot{D}(t)*B(t;T_r)$$

Haskell source model: far field

$$u_r(r,t) \propto \dot{D}(t) * v_r H(z)\Big|_{t-x/v_r}^{t} = v_r \dot{D}(t) * B(t;T_r)$$

resulting in the convolution of two boxcars: the first with duration equal to the rise time and the second with duration equal to the **rupture time** (L/v_r)

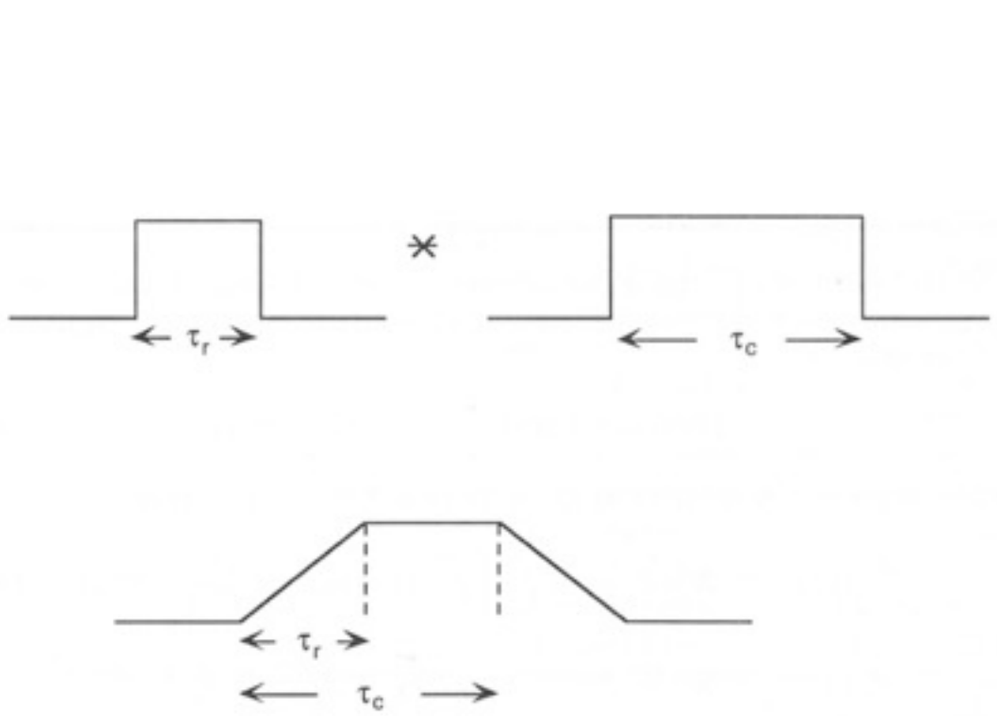

FIGURE 9.6 The convolution of two boxcars, one of length τ_r and the other of length τ_c ($\tau_c > \tau_r$). The result is a trapezoid with a rise time of τ_r, a top of length $\tau_c - \tau_r$, and a fall of width τ_r.

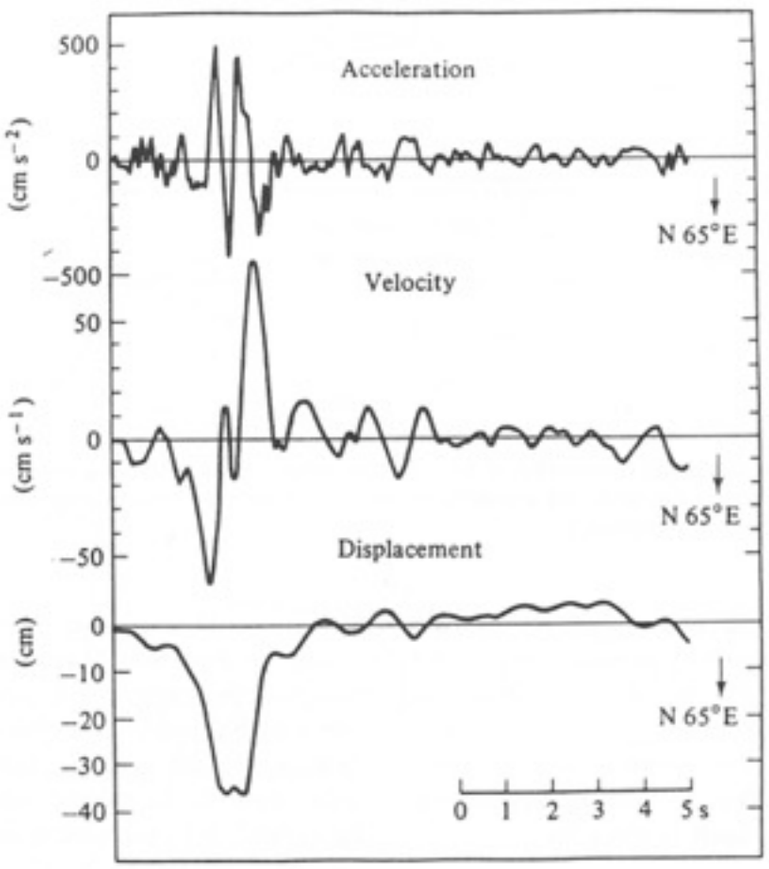

FIGURE 9.7 A recording of the ground motion near the epicenter of an earthquake at Parkfield, California. The station is located on a node for *P* waves and a maximum for *SH*. The displacement pulse is the *SH* wave. Note the trapezoidal shape. (From Aki, *J. Geophys. Res.* 73, 5359–5375, 1968; © copyright by the American Geophysical Union.)

Haskell source model: directivity

The body waves generated from a breaking segment will arrive at a receiver before than those that are radiated by a segment that ruptures later.
If the path to the station is not perpendicular, the waves generated by different segments will have different path lengths, and then unequal travel times.

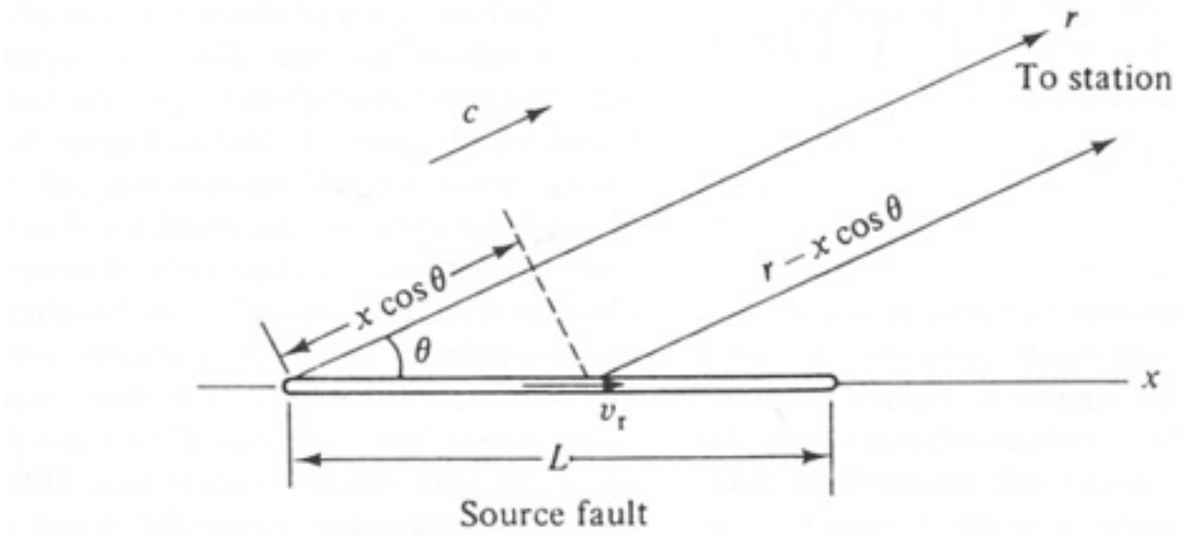

FIGURE 9.8 Geometry of a rupturing fault and the path to a remote recording station. (From Kasahara, 1981.)

$$T_r = \left[\frac{L}{v_r} + \left(\frac{r - L\cos\theta}{c}\right)\right] - \frac{r}{c} =$$

$$= \frac{L}{v_r} - \left(\frac{L\cos\theta}{c}\right) = \frac{L}{v_r}\left(1 - \frac{v_r}{c}\cos\theta\right)$$

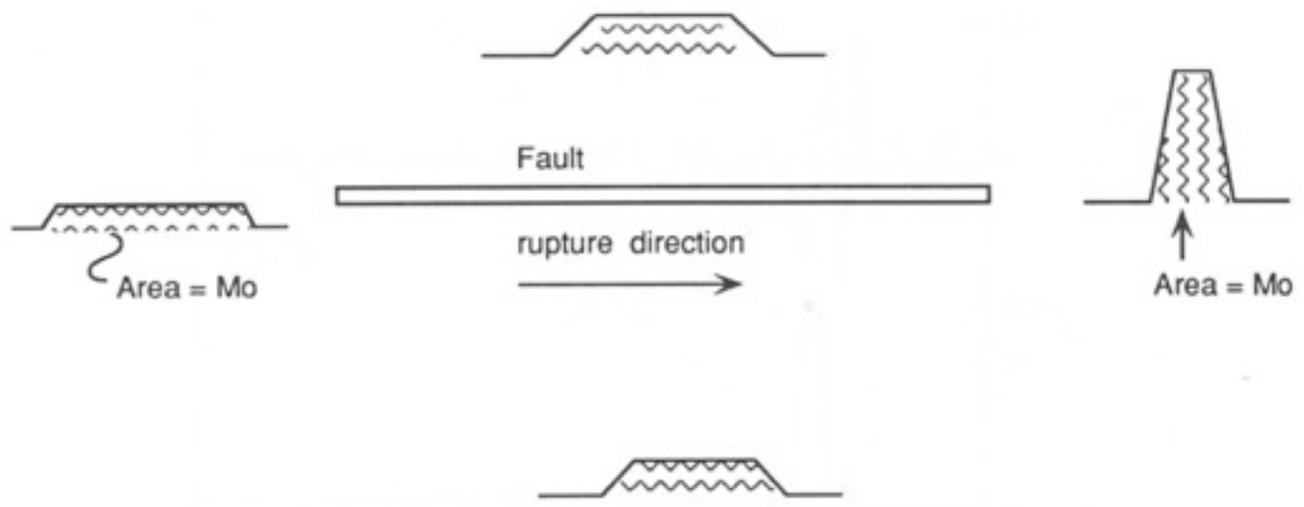

FIGURE 9.9 Azimuthal variability of the source time function for a unilaterally rupturing fault. The duration changes, but the area of the source time function is the seismic moment and is independent of azimuth.

Rupture velocity

Earthquake ruptures typically propagate at velocities that are in the range 70–90% of the S-wave velocity and this is independent of earthquake size. A small subset of earthquake ruptures appear to have propagated at speeds greater than the S-wave velocity. These supershear earthquakes have all been observed during large strike-slip events.

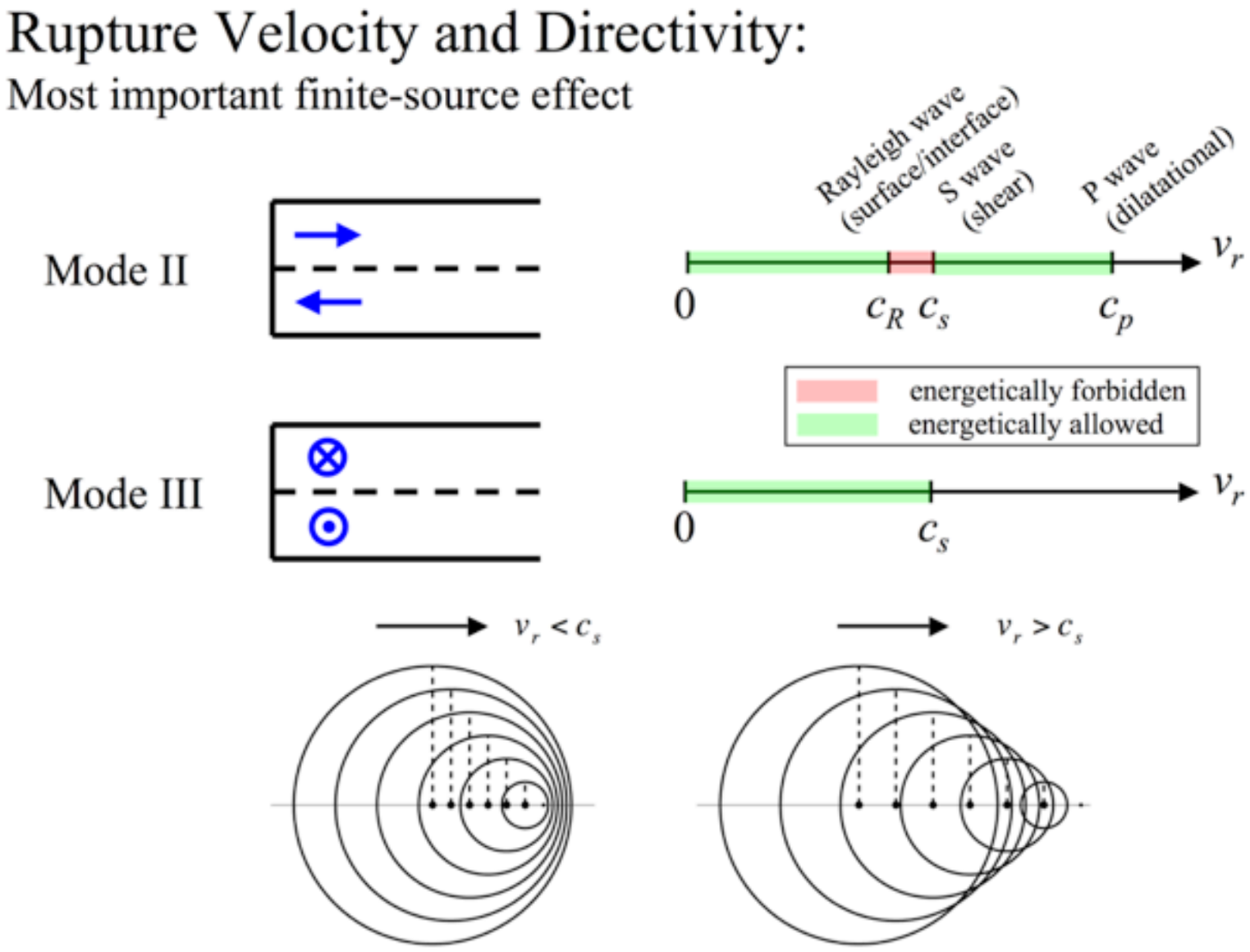

http://pangea.stanford.edu/~edunham/research/supershear.html

Directivity example

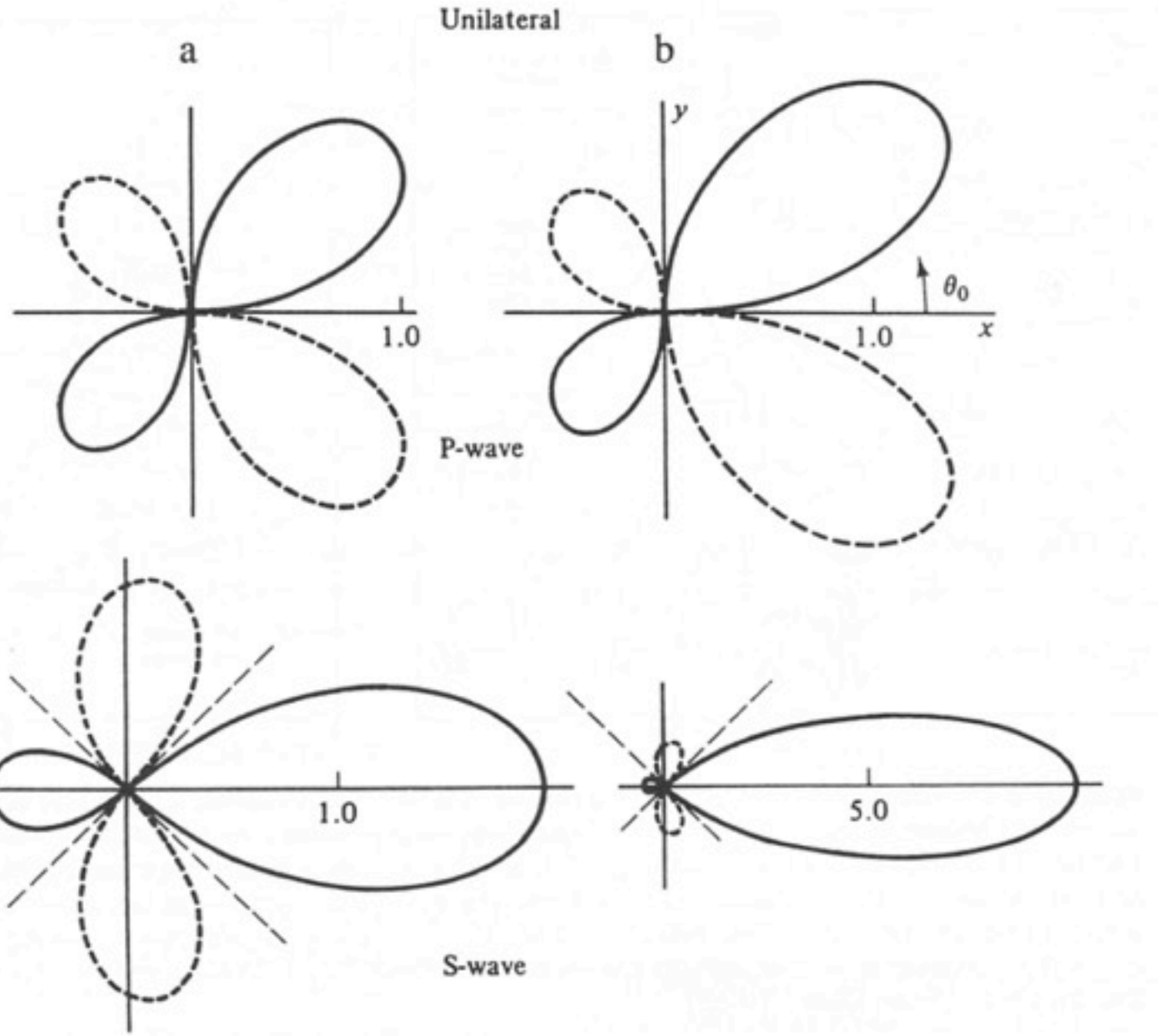

FIGURE 9.10 The variability of *P*- and *SH*-wave amplitude for a propagating fault (from left to right). For the column on the left $v_r/v_s = 0.5$, while for the column on the right $v_r/v_s = 0.9$. Note that the effects are amplified as rupture velocity approaches the propagation velocity. (From Kasahara, 1981.)

Ground motion scenarios

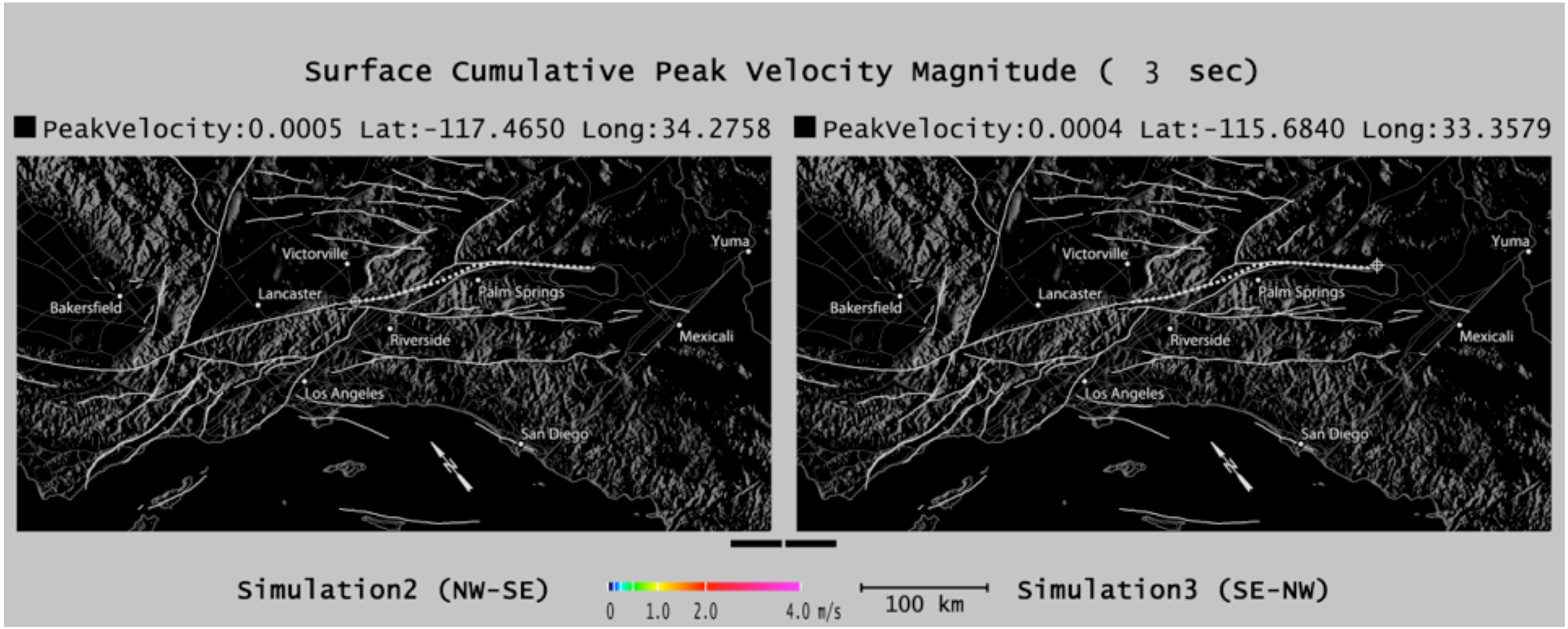

The two views in this movie show the cumulative velocities for a San Andreas earthquake TeraShake simulation, rupturing south to north and north to south. The crosshairs pinpoint the peak velocity magnitude as the simulation progresses.

www.scec.org

Source spectrum

The displacement pulse, corrected for the geometrical spreading and the radiation pattern can be written as:

$$u(t) = M_0\left(B(t;\tau) * B(t;T_R)\right)$$

and in the frequency domain:

$$U(\omega) = M_0 F(\omega) = M_0 \left|\frac{\sin\left(\frac{\omega\tau}{2}\right)}{\left(\frac{\omega\tau}{2}\right)}\right| \left|\frac{\sin\left(\frac{\omega L}{v_r 2}\right)}{\left(\frac{\omega L}{v_r 2}\right)}\right| \approx \begin{cases} M_0 & \omega < \frac{2}{T_r} \\ \frac{2M_0}{\omega T_R} & \frac{2}{T_r} < \omega < \frac{2}{\tau} \\ \frac{4M_0}{\omega^2 \tau T_R} & \omega > \frac{2}{\tau} \end{cases}$$

Source spectrum

$$U(\omega) \approx \begin{cases} M_0 & \omega < \dfrac{2}{T_r} \\ \dfrac{2M_0}{\omega T_R} & \dfrac{2}{T_r} < \omega < \dfrac{2}{\tau} \\ \dfrac{4M_0}{\omega^2 \tau T_R} & \omega > \dfrac{2}{\tau} \end{cases}$$

Figure 4.6-4: Approximation of the (sin *x*)/*x* function, and derivation of corner frequencies.

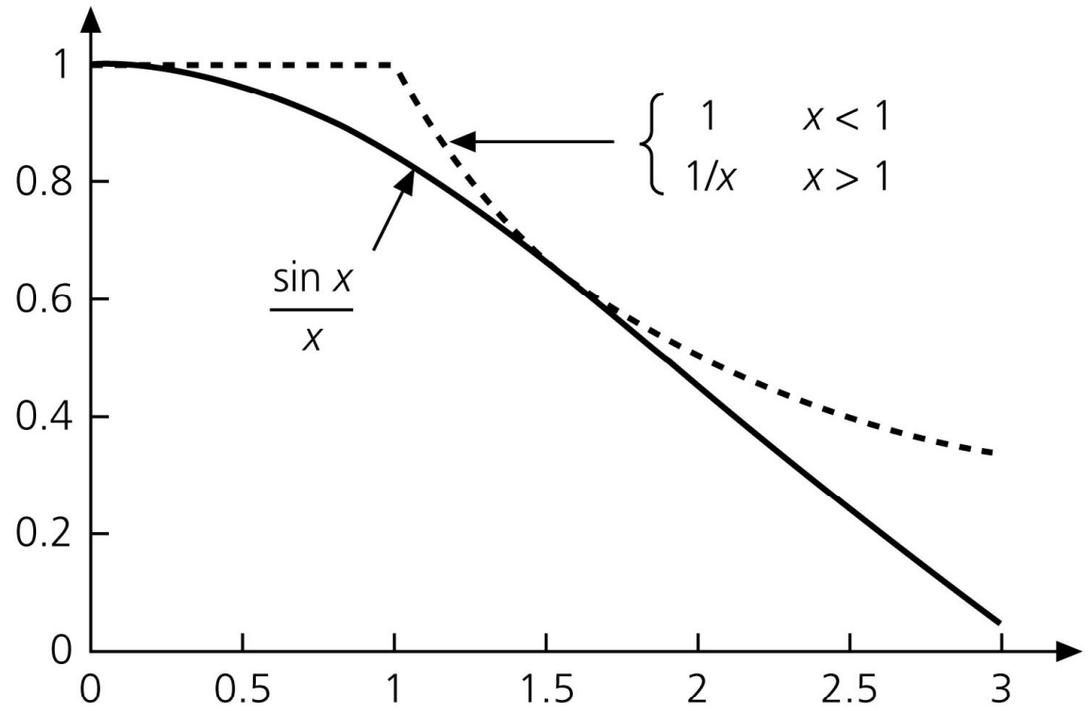

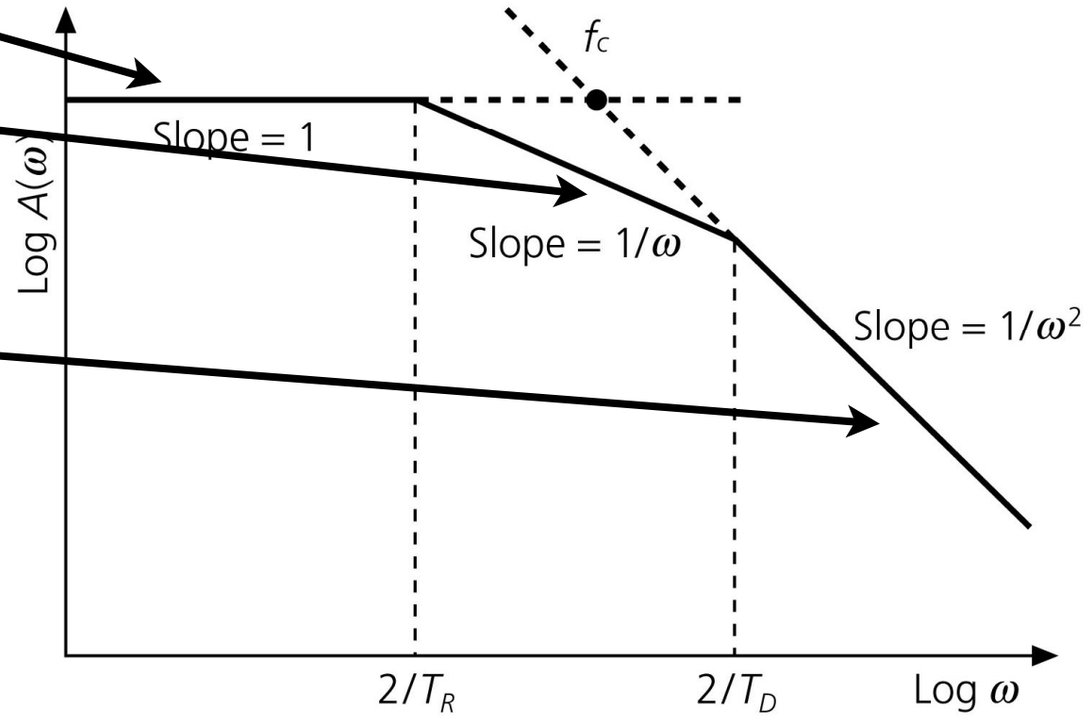

Empirical source spectra

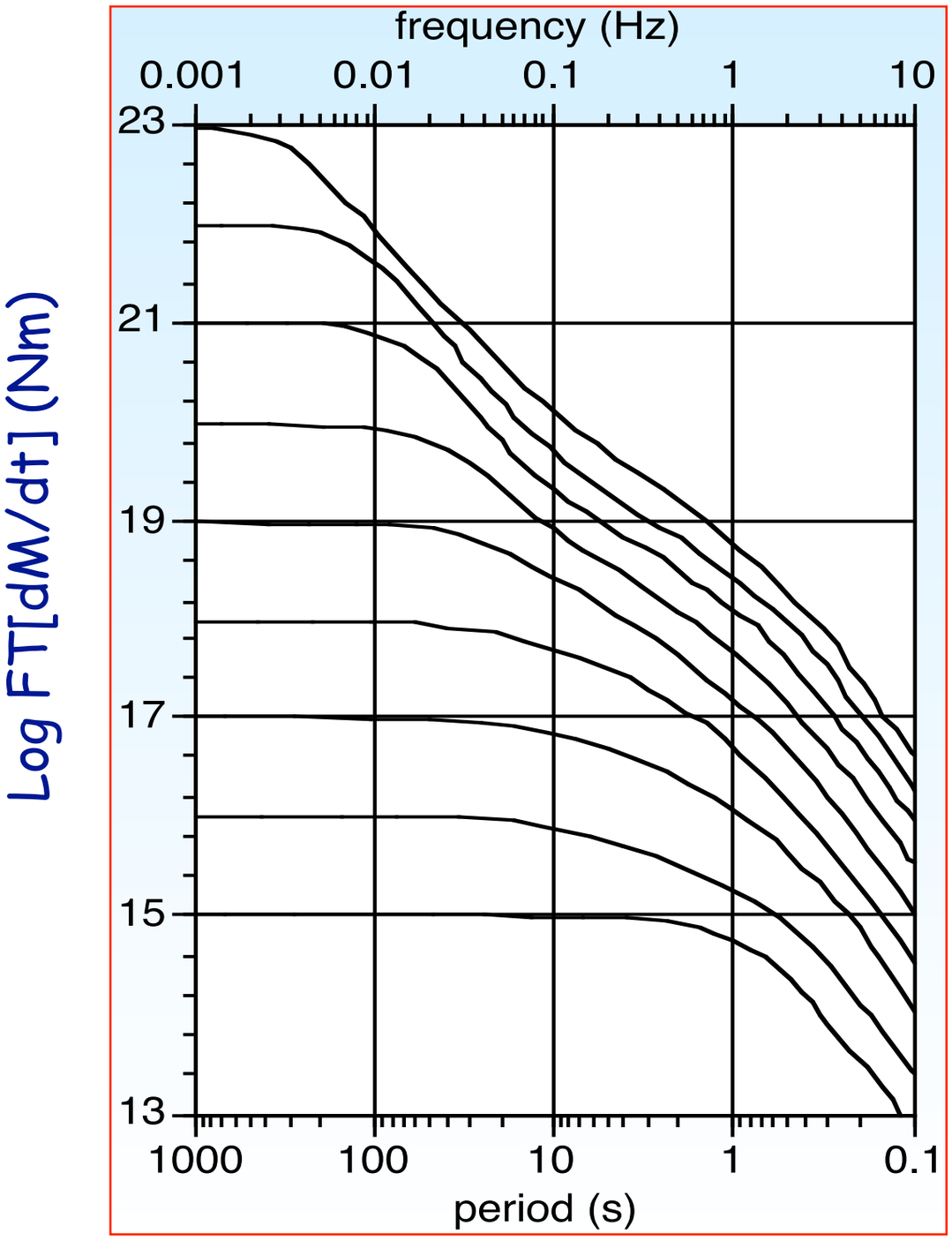

Empirical source spectra

represent a set of average amplitude curves respect to:

Tectonic setting

Source mechanism

Directivity effects